Geometrically Exact Kirchhoff Beam Theory: Application to cable dynamics

Frédéric Boyer, Guillaume de Nayer, Alban Leroyer, Michel Visonneau

Geometrically Exact Kirchhoff Beam Theory: Application to Cable Dynamics

Frédéric Boyer
Institut de Recherche en Communications et Cybernétique de Nantes (IRCCyN), Ecole des Mines de Nantes, France

Guillaume De Nayer
Fakultät für Maschinenbau, Helmut-Schmidt Universität, Holstenhofweg 85, Hamburg, Germany

Alban Leroyer, Michel Visonneau
Laboratoire de Mécanique des Fluides, UMR CNRS 6598, Ecole Centrale de Nantes, France

In this article, the finite element simulation of cables is investigated for future applica-tions to robotics and hydrodynamics. The solution is based on the geometrically exact approach of Cosserat beams in finite transformations, as initiated by Simo in the 1980s. However, the internal basic kinematics of the beam theory is not those of Reissner–Timoshenko but rather those of Kirchhoff. Based on these kinematics, the dynamic model adopted is a nonlinear extension of the so-called linear model of twisted and stretched Euler–Bernoulli beams. In agreement with the investigated applications, one or both of the ends of the cable are submitted to predefined motions. This model is also implemented into a computational fluid dynamics code, which solves the Reynolds-averaged Navier–Stokes equations. Regarding this last point, an implicit/iterative algorithm including a conservative load transfer for the variable hydrodynamic forces exerted all along the beam length has been used to reach a stable coupling. The relevance of the approach is tested through three advanced examples. The first is related to the prediction of cable motion in robotics. Then, the two last illustrations deal with fluid-structure interaction (FSI). A 2D classical benchmark in FSI is first investigated, and, at last, a computation illustrates the procedure in a 3D case.

Keywords: nonlinear Kirchhoff beam, geometrically exact, finite elements, cable, FSI, computational fluid dynamics

1 Introduction

Cables and other flexible pipes are found in many applications of civil, aerospace, and mechanical engineering. They are also commonly used in robotics, to bring energy to the actuators of a robotic arm. In oceanic engineering, risers are used, for example, to convey fluids from the bottom of the sea up to the surface. In these applications, engineers need numerical models of nonlinear thin deformable structures in order to predict their motions and the internal stress they undergo for a given application. Hence, the need for numerical nonlinear beam models is still an intense subject of research. Among the most advanced finite element methods proposed for nonlinear beams, the geometrically exact approach initiated by Simo is probably one of the most efficient. This approach is based on the Cosserat assumption of rigid cross sections [1] and on Timoshenko's internal kinematics [2], as extended to finite transformations by Reissner [3]. Following the pioneering work of Simo [4], Simo and Vu-Quoc [5,6], and Cardona and Gérardin [7], this approach was further improved through the work of Cardona et al. [8], Ibrahimbegovic et al. [9], Ibrahimbegovic [10], Ibrahimbegovic and Al Mikdad [11], Ibrahimbegovic and Mamouri [12], Chrisfield and Jelenic [13], Kapania and Li [14], and Zupan and Saje [15]. As regards numerical performances, the good results of this approach are essentially due to the fact that it requires no approximation of the finite rotations of the cross sections except the unavoidable discretization of the structure domain into finite elements and of the time axis through the integration schemas [16].

However, when the "length/thickness" ratio of the beam becomes very high (i.e., when the structure is more of a rope or a cable than a beam), it becomes relevant to use the alternative internal kinematics of Kirchhoff and Clebsch [17], as is done in oceanic engineering for the simulation of very long undersea cables [18–21].

Based on the nonlinear Kirchhoff beam theory, much progress has been accomplished by the oceanic engineering community. However, most of the results related to undersea cables have been based to date on the finite difference methods (see Refs. [18–21]) with a very few based on the usual (not geometrically exact) finite element method [22].

Hence, developing geometrically exact finite element methods for cables is still a relevant challenge in nonlinear structural dynamics. A first step toward this goal was made in Ref. [23], where a geometrically exact finite element method based on Kirchhoff kinematics is proposed. In this reference, two models are tested and compared with the Reissner–Simo model. Prolonging the linear beam theory, these models correspond to those of Euler–Bernoulli and Rayleigh [24]. In comparison to the geometrically exact theory of Reissner–Timoshenko beams, these models are not defined on the same configuration space since, in the case of very slender beams, the orthonormal frames of the Reissner theory reduce to the field of the unit vectors tangent to the line of centroids, i.e., in the language of Cosserat media, a continuous set of directors [25,26]. This difference requires replacing the Lie group $SO(3)$ of the configuration space of Reissner theory by the fibration $S^2 \times SO(2)$ [27], where $S^2 = SO(3)/SO(2)$ stands for the orientation of the cross section normals, which is parameterized by the position field of the centroid line while $SO(2)$ stands for the cross section roll around the centroid line. In the current article, the geometrical approach is applied to this definition of the configuration space in order to address the problem of the modeling and simulation of cables with a view to future application to the detection of collisions in robotics and to the installation of risers in oceanic engineering. In particular, this article proposes a model (and its finite element implementation) of a nonlinear Euler–Bernoulli beam whose ends are possibly controlled by imposed

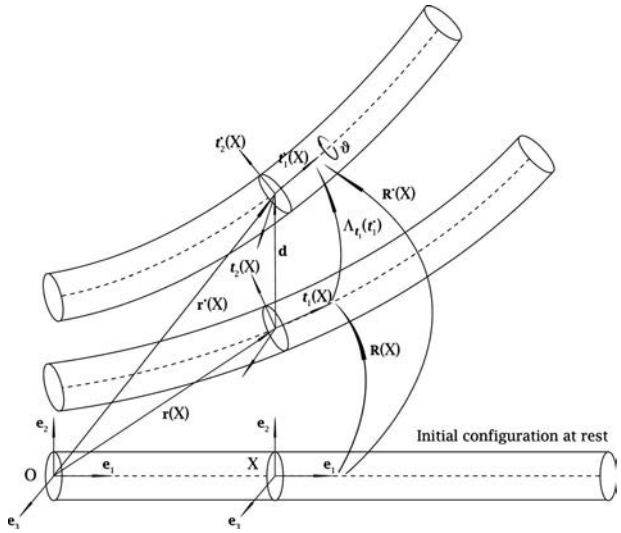

Fig. 1 Basic kinematics of a beam

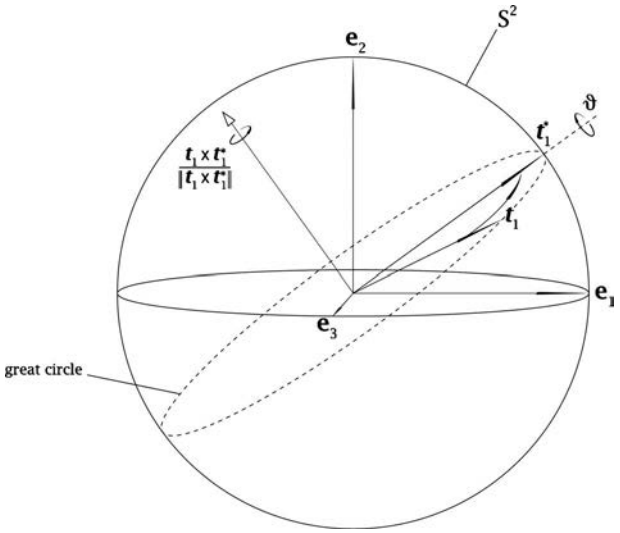

Fig. 2 Parameterization of the rotation field

motion and submitted to external forces (gravity and fluid forces). The constraints are modeled through an augmented Lagrangian approach with penalty, consistent with the Kirchhoff parameterization. Furthermore, this beam solver is coupled to a computational fluid dynamics (CFD) code, enabling complex vortex induced vibration (VIV) configurations to be handled.

This article is structured as follows. We first start by establishing the basic kinematics of the cable and the parameterization of its configuration space (Sec. 2). Once the geometric model has been achieved, we derive, in Sec. 3, the weak forms of the dynamics of a cable constrained at its two ends to follow some imposed motions. Then, the numerical algorithm is explained in Sec. 4. It is based on a Newmark implicit integrator coupled to a Newton resolution algorithm of the resulting algebraic formulation. Finally, the algorithm must be completed with a finite element discretization (Sec. 5) and some updated formulae of the weak form and its linearization. This is the purpose of Sec. 6. In Sec. 7, the approach is illustrated by some simulation results obtained on three examples. The first is related to predicting the motion of a cable linked to a moving robot arm. The second one concerns the fluid-structure interaction (FSI) application field: The main steps of the flow/motion coupling with a CFD solver are first described, followed by a classical benchmark of a 2D filament clamped behind a square rigid body and then submitted to a VIV phenomenon. As the previous test-case, the third one is a FSI illustration: It was done to show the capabilities of the FSI code in 3D.

2 Basic Kinematics and Parameterization of the Cable Geometry

The ambient space is given by a fixed Cartesian frame $(O,\mathbf{e}_1,\mathbf{e}_2,\mathbf{e}_3)$. Throughout this article, the tensor product will be denoted by $\otimes$, the contracted product of tensors by a point, and for any $\mathbf{V}\in\mathbb{R}^3$, $\hat{\mathbf{V}}=\mathbf{V}\hat{}\in\mathbb{R}^3\otimes\mathbb{R}^3$ will be the skew symmetric tensor such that $\forall\mathbf{x}\in\mathbb{R}^3:\mathbf{V}\times\mathbf{x}=\hat{\mathbf{V}}\cdot\mathbf{x}$. We consider a cable with a constant circular cross section and suppose it to be straight when at rest. We denote by X, the material abscissa along the cable and by $(\mathbf{t}_i(t,X))_{i=1,2,3}$, the moving orthonormal frame rigidly attached to the X cross section (centered on its center of gravity) and such that $\mathbf{t}_1$ supports the material axis of the cable (see Fig. 1). At $t=0$, the cable is at rest, and such that its material axis (centroidal line) is along $(O,\mathbf{e}_1)$, i.e., $(\mathbf{t}_i(0,X)=\mathbf{e}_i)_{i=1,2,3}$. Adopting the Euler–Bernoulli model of thin beams, the cross sections remain orthogonal to the centroidal line (Kirchhoff assumption). Consequently, any transformation undergone by the cable can be parameterized by the composition of a translation changing the position field $X\mapsto\mathbf{r}(X)$ into $X\mapsto\mathbf{r}^*(X)=\mathbf{r}(X)+\mathbf{d}(X)$ (where $\mathbf{d}$ is a displacement field), and a rotation changing the orientation field $X\mapsto\mathbf{R}(X)$ with respect to the configuration at rest into (see Fig. 2)

$$\mathbf{R}^*(X)=\exp(\vartheta\hat{\mathbf{t}}_1^*)\mathbf{\Lambda}_{\mathbf{t}_1}(\mathbf{t}_1^*)\mathbf{R}(X) \tag{1}$$

where we introduce the field of unit tangent to the reference line after the transformation $X\mapsto\mathbf{t}_1^*(X)=\partial_X\mathbf{r}^*/\|\partial_X\mathbf{r}^*\|$ and the following rotation compatible with the Kirchhoff assumption:[1]

$$\mathbf{\Lambda}_{\mathbf{t}_1}(\mathbf{t}_1^*)=(\mathbf{t}_1\cdot\mathbf{t}_1^*)\mathbf{I}_3+\frac{1}{1+\mathbf{t}_1\cdot\mathbf{t}_1^*}(\mathbf{t}_1\times\mathbf{t}_1^*)\otimes(\mathbf{t}_1\times\mathbf{t}_1^*)+(\mathbf{t}_1\times\mathbf{t}_1^*)\hat{} \tag{2}$$

which is the unique rotation applying $\mathbf{t}_1\in S^2$ onto $\mathbf{t}_1^*\in S^2$ while leaving the unit vector $\mathbf{t}_1\times\mathbf{t}_1^*/\|\mathbf{t}_1\times\mathbf{t}_1^*\|$ invariant [28,29]. Finally, $\exp(\vartheta\hat{\mathbf{t}}_1^*)$, where "exp" denotes the exponential of matrices,[2] is the rotation about the vector $\mathbf{t}_1^*$ of an angle ϑ, which stands for a roll angle about the centroidal line. Once such a set of transformations is defined, we can use it to parameterize the configuration space of the cable. For that, we just distinguish a configuration $\mathbf{\Phi}=(\mathbf{r},\mathbf{R})$ of the cable and define any other configuration $\mathbf{\Phi}^*=(\mathbf{r}^*,\mathbf{R}^*)$ as the action onto this arbitrary configuration (said to be "of reference") of any transformation of the form $(\mathbf{d},\exp(\vartheta\hat{\mathbf{t}}_1^*)\mathbf{\Lambda}_{\mathbf{t}_1}(\mathbf{t}_1^*))\in\mathbb{R}^3\times SO(3)$. In the numerical treatment that follows, the reference configuration is not fixed once and for all but updated at each time step of the simulation. Such a choice corresponds to the so-called updated Lagrangian approach of nonlinear elasticity and has to be distinguished from the "total Lagrangian" approach, where the reference configuration is unique and usually coincides with the initial one. This choice is adopted in order to avoid the singularity of Eq. (2), which occurs when $\mathbf{t}_1=-\hat{\mathbf{t}}_1^*$. As a matter of fact, this singularity corresponds to an antipodal (related on S^2) rotation of the cross section, easily avoidable by updating the reference configuration sufficiently often. Finally, in this approach, the current rotation field $\mathbf{R}(t,.):X\mapsto\mathbf{R}(t,X)$ will be parameterized as

[1] Referring to Riemannian geometry, any $\mathbf{\Lambda}_\mathbf{u}(\mathbf{v})$ defines on the unit sphere S^2, the action of the parallel transport of the Levi–Civita connection along the geodesic (great circle) linking $\mathbf{u}\in S^2$ with $\mathbf{v}\in S^2$.

[2] Given in the case of $SO(3)$ by $\exp(\hat{\mathbf{v}})=\cos(\|\mathbf{v}\|)\mathbf{I}_3+(1-\cos(\|\mathbf{v}\|))(\mathbf{v}/\|\mathbf{v}\|)\otimes(\mathbf{v}/\|\mathbf{v}\|)+\sin(\|\mathbf{v}\|)(\mathbf{v}/\|\mathbf{v}\|)\hat{}$.

$$\mathbf{R}(t,X) = \exp(\vartheta(t,X)\hat{\mathbf{t}}_1(t,X))\mathbf{\Lambda}_{\mathbf{t}_{1n}}(\mathbf{t}_1(t,X))\mathbf{R}_n(X) \tag{3}$$

where $\mathbf{t}_{1n}(X) = \partial_X \mathbf{r}_n / \|\partial_X \mathbf{r}_n\|$ and $\mathbf{r}_n$ stands for the position field of the centroidal line at the last time step t_n, where the equilibrium has been numerically reached by the algorithm. In the same manner, $\mathbf{R}_n(X)$ is the orientation tensor of the X cross section at time t_n measured with respect to the initial straight configuration.

3 Governing Balance Equations: Weak Form

In what follows, we denote by a prime symbol and a dot symbol, the operators ∂_X and ∂_t, respectively, and suppose the material abscissa of the beam normalized ($X \in [0,1]$).

3.1 Strain and Stress Fields. In the framework of finite displacements and small strains and under the Kirchhoff assumption, the strain state of the cable is defined by the three following fields (a vector with the subscript $\perp$ (respectively, with a $\|$) is normal (respectively, parallel) to the beam axis.

1. The vector field of curvature $\mathbf{k}_\perp : X \mapsto \mathbf{t}_1' = (\mathbf{t}_1' \cdot \mathbf{t}_2)\mathbf{t}_2 + (\mathbf{t}_1' \cdot \mathbf{t}_3)\mathbf{t}_3$.
2. The scalar field of torsion $K : X \mapsto K = \mathbf{t}_2' \cdot \mathbf{t}_3 = -\mathbf{t}_3' \cdot \mathbf{t}_2$.
3. The scalar field of stretching $\xi : X \mapsto \xi = \|\mathbf{r}'\| - 1$, where we note that we have the following subsidiary relation:

$$\mathbf{R}'\mathbf{R}^T = (\mathbf{k}_\perp + K\mathbf{t}_1)\hat{} = (\mathbf{k}_\perp + \mathbf{k}_\|)\hat{}$$

and that these strain measurements verify the material objectivity [30] required by the modeling of finite displacements.

On the dual side, we have the following internal force and torque densities per unit of beam length (the convention on repeated subscript $\alpha = 2,3$ is adopted):

$$\mathbf{m} = M\mathbf{t}_1 + M_\alpha \mathbf{t}_\alpha = \mathbf{m}_\| + \mathbf{m}_\perp, \quad \mathbf{n} = N\mathbf{t}_1 + N_\alpha \mathbf{t}_\alpha = \mathbf{n}_\| + \mathbf{n}_\perp$$

Finally, occurring in the framework of small strains and material elasticity, the internal stress and strains are related by the reduced Hook's law [4]

$$\mathbf{m}_\| = GI_p K\mathbf{t}_1, \quad \mathbf{m}_\perp = EI_a \mathbf{t}_1', \quad \mathbf{n}_\| = EA\xi\mathbf{t}_1$$

with EI_a, GI_p, and EA as the bending stiffness, twisting stiffness, and stretching stiffness per unit of beam length, respectively.

3.2 Statement of the Variational Formulation. For the moment, we only consider the case where the external conservative forces are due to gravity, and we will consider more general nonconservative forces at the end of the section. Under the Euler–Bernoulli assumption, the rotational kinetic energy of cross sections is neglected and the Lagrangian of the free cable (without constraint) is simply

$$L_f = \frac{1}{2}\int_0^1 \rho A \dot{\mathbf{r}}^2 dX - \frac{1}{2}\int_0^1 EI_a \mathbf{t}_1'^2 dX - \frac{1}{2}\int_0^1 GI_p K^2 dX - \frac{1}{2}\int_0^1 EA\xi^2 dX - \frac{1}{2}\int_0^1 \rho A \mathbf{g}\cdot\mathbf{r} dX \tag{4}$$

where, from left to right, we find the kinetic energy of the cable, its bending energy, its torsion and stretching energies and, finally, the potential energy due to gravity ($\mathbf{g}$ and ρA are the gravity acceleration field and the mass density per unit of beam length, respectively).

In what follows, we consider the case of a cable constrained at one or both of its ends to follow some imposed motions. Thus, for a given cable configuration $\mathbf{\Phi} = (\mathbf{r}, \mathbf{R})$ with $\mathbf{R}$ in the form Eq. (3), the geometric constraints at the two ends take the form

$$\mathbf{\Upsilon}(\mathbf{\Phi},t) = \begin{bmatrix} \mathbf{\Upsilon}_0(\mathbf{\Phi},t) \\ \mathbf{\Upsilon}_1(\mathbf{\Phi},t) \end{bmatrix} = \mathbf{0}, \quad \text{with } \mathbf{\Upsilon}_X(\mathbf{\Phi},t) = \begin{bmatrix} \mathbf{r}(X) - \mathbf{r}_d(X,t) \\ \mathbf{r}'(X) - \mathbf{r}_d'(X,t) \\ \vartheta(X) - \vartheta_d(X,t) \end{bmatrix} \tag{5}$$

The case with only one constrained end is a particular subcase, where $\mathbf{\Upsilon}_0$ (respectively, $\mathbf{\Upsilon}_1$) has to be canceled. In $\mathbf{\Upsilon}_X$, the first (from top to bottom) set of constraints imposes a desired position of the X cross section while the next two (with ϑ defined by 3 for a field of arbitrary reference orientations $\mathbf{R}_n$) completely specify its orientation. With these constraints, we define the augmented Lagrangian of the cable

$$L_+ = L_f + \boldsymbol{\lambda}\cdot\mathbf{\Upsilon} \tag{6}$$

where we introduced the vector of Lagrange multipliers $\boldsymbol{\lambda} = (\boldsymbol{\lambda}^T(0), \boldsymbol{\lambda}^T(l))^T$ with $\boldsymbol{\lambda}(X) = (\boldsymbol{\lambda}_{\mathbf{r}}^T(X), \boldsymbol{\lambda}_{\mathbf{r}'}^T(X), \lambda_\vartheta(X))^T$.

The Hamilton principle of constrained systems postulates that the motion of the cable makes the augmented action stationary [8], i.e.,

$$\delta\int_{t_1}^{t_2} L_+ dt = 0, \quad \forall\ \delta\mathbf{\Phi},\ \forall\ \delta\boldsymbol{\lambda} \tag{7}$$

where $\delta\mathbf{\Phi} = (\delta\mathbf{r}, \delta\mathbf{R})$ and $\delta\mathbf{R}$ are compatible with Kirchhoff kinematics; it has to verify the infinitesimal version[3] of Eq. (1)

$$\delta\mathbf{R} = \left.\frac{d}{d\epsilon}\right|_{\epsilon=0} (\exp(\epsilon\delta\theta\hat{\mathbf{t}}_1)\mathbf{\Lambda}_{\mathbf{t}_1}(\mathbf{t}_{1,\epsilon})\mathbf{R}) = (\delta\theta\mathbf{t}_1 + \mathbf{t}_1 \times \delta\mathbf{t}_1)\hat{}\,\mathbf{R} \tag{8}$$

where we introduce the scalar field of variation $\delta\theta = \delta\mathbf{t}_2\cdot\mathbf{t}_3 = -\delta\mathbf{t}_3\cdot\mathbf{t}_2$, and where the fields subscripted by ϵ are deduced from those nonsubscripted by substituting the field $\mathbf{r}$ by its perturbation $\mathbf{r}_\epsilon = \mathbf{r} + \epsilon\delta\mathbf{r}$ into their definition. As the variation is achieved with fixed time and ends, Eq. (7) details as

$$\int_{t_1}^{t_2} \delta L_f + \delta\mathbf{\Upsilon}\cdot\boldsymbol{\lambda} + \delta\boldsymbol{\lambda}\cdot\mathbf{\Upsilon} dt = 0, \quad \forall\ \delta\mathbf{\Phi},\ \forall\ \delta\boldsymbol{\lambda} \tag{9}$$

Moreover, computing the variation of Eq. (3) with $\vartheta_\epsilon = \vartheta + \epsilon\delta\vartheta$, and identifying the result with Eq. (8), gives

$$\delta\mathbf{R} = (\delta\theta\mathbf{t}_1 + \mathbf{t}_1 \times \delta\mathbf{t}_1)\hat{}\,\mathbf{R} = \left.\frac{d}{d\epsilon}\right|_{\epsilon=0} (\exp(\vartheta_\epsilon\hat{\mathbf{t}}_{1,\epsilon})\mathbf{\Lambda}_{\mathbf{t}_{1n}}(\mathbf{t}_{1,\epsilon})\mathbf{R}_n)$$

After computation, we find the following scalar relation, which links the iterative roll angle $\delta\theta$ with the incremental one $\delta\vartheta$:

$$\delta\vartheta = \delta\theta + \mathbf{u}_n(X)\cdot\delta\mathbf{r}' \tag{10}$$

where we introduced the vector field

$$\mathbf{u}_n = \frac{\mathbf{t}_{1n} \times \mathbf{t}_1}{\|\mathbf{r}'\|(1 + \mathbf{t}_{1n}\cdot\mathbf{t}_1)} \tag{11}$$

Then, inserting Eq. (10) into $\delta\mathbf{\Upsilon}\cdot\boldsymbol{\lambda}$ of Eq. (9) allows one to write

$$\delta L_+ = \delta L_f + \begin{bmatrix} \delta\mathbf{r}(0) \\ \delta\mathbf{r}'(0) \\ \delta\theta(0) \end{bmatrix} \cdot \mathbf{f}_c(0) + \begin{bmatrix} \delta\mathbf{r}(1) \\ \delta\mathbf{r}'(1) \\ \delta\theta(1) \end{bmatrix} \cdot \mathbf{f}_c(1) + \delta\boldsymbol{\lambda}\cdot\mathbf{\Upsilon} = 0 \tag{12}$$

where we introduce the following generalized forces induced by the constraints:

[3] $d/d\epsilon|_{\epsilon=0}$ denotes the directional (Gateau) derivative.

$$\mathbf{f}_c = \begin{bmatrix} \boldsymbol{\lambda}_{\mathbf{r}} \\ \boldsymbol{\lambda}_{\mathbf{r}'} + \lambda_\vartheta \mathbf{u}_n \\ \lambda_\vartheta \end{bmatrix} \tag{13}$$

Finally, the variation of K is defined by

$$\delta K = \left.\frac{d}{d\epsilon}\right|_{\epsilon=0} (\mathbf{t}'_{2,\epsilon} \cdot \mathbf{t}_{3,\epsilon}) = - \left.\frac{d}{d\epsilon}\right|_{\epsilon=0} (\mathbf{t}'_{3,\epsilon} \cdot \mathbf{t}_{2,\epsilon})$$

and after computation, it can be detailed as

$$\delta K = \delta\theta' + \left(\frac{\mathbf{t}_1 \times \mathbf{t}'_1}{\|\mathbf{r}'\|}\right) \cdot \delta\mathbf{r}' \tag{14}$$

Now, let us apply the extended Hamilton principle

$$\delta \int_{t_1}^{t_2} L_+ dt = \int_{t_1}^{t_2} \delta W_{\text{ext}} dt, \quad \forall\ \delta\boldsymbol{\Phi},\ \forall\ \delta\boldsymbol{\lambda} \tag{15}$$

where δW_{ext} is the virtual work produced by an eventual field of nonconservative external fluid forces (such as those applied on an underwater cable). Such a field of forces will be approximated through a wrench density of follower loads of the form

$$[0,1] \to \mathbb{R}^3 \times SO(3)^*$$

$$X \mapsto (\bar{\mathbf{n}}, \bar{\mathbf{m}}) = (\bar{N}_i \mathbf{t}_i, \bar{M}_i \mathbf{t}_i) \tag{16}$$

where $\bar{N}_i$ and $\bar{M}_i$ for $i=1,2,3$ are considered in the following as explicit time-dependent functions. Finally, by inserting Eq. (14) into Eq. (15) and achieving standard integrations by parts, the set of partial differential equations (PDEs) in the Cauchy form (i.e., the strong form of a nonlinear Euler–Bernoulli clamped at both ends) could be written. Since numerical applications are involved in this paper, only the weak form is under consideration in what follows.

3.3 Weak Form of Virtual Works. Now, let us consider the following Lagrangian:

$$L_+ = L_f + \boldsymbol{\lambda} \cdot \boldsymbol{\Upsilon} + \frac{p}{2} \boldsymbol{\Upsilon} \cdot \boldsymbol{\Upsilon} \tag{17}$$

where we add to Eq. (6) a penalty term (p is an arbitrary factor) in order to improve the convergence of the subsequent algorithm [8]. Then, repeating the same calculus as before (starting again from Eq. (15)) but without achieving the spatial integration by parts,[4] we obtain the weak form of virtual works that will be used later to solve the finite element formulation

$$\int_0^1 \begin{bmatrix} \delta\mathbf{r} \\ \delta\mathbf{r}' \\ \delta\theta \end{bmatrix} \cdot (\mathbf{f}_{\text{dyn}} - \mathbf{f}_g - \mathbf{f}_{\text{ext}}) dX + \int_0^1 \begin{bmatrix} \delta\mathbf{r}' \\ \delta\mathbf{r}'' \\ \delta\theta' \end{bmatrix} \cdot \mathbf{f}_{\text{stat}} dX + \delta\boldsymbol{\Upsilon} \cdot (\boldsymbol{\lambda} + p\boldsymbol{\Upsilon}) + \delta\boldsymbol{\lambda} \cdot \boldsymbol{\Upsilon} = 0 \tag{18}$$

where

$$(\mathbf{f}_{\text{dyn}} - \mathbf{f}_g - \mathbf{f}_{\text{ext}})^T = \left(\rho A(\ddot{\mathbf{r}} - \mathbf{g})^T - \bar{\mathbf{n}}^T, -\frac{(\bar{\mathbf{m}} \times \mathbf{t}_1)^T}{\|\mathbf{r}'\|}, -\mathbf{t}_1 \cdot \bar{\mathbf{m}}\right) \tag{19}$$

and

$$\mathbf{f}_{\text{stat}} = \begin{bmatrix} EA\left(1 - \frac{1}{\|\mathbf{r}'\|}\right)\mathbf{r}' + EI_a\left(2\frac{(\mathbf{r}' \cdot \mathbf{r}'')^2}{\|\mathbf{r}'\|^6} - \frac{(\mathbf{r}' \cdot \mathbf{r}'')\mathbf{r}'' + \|\mathbf{r}''\|^2 \mathbf{r}'}{\|\mathbf{r}'\|^4}\right) \\ EI_a\left(\frac{\mathbf{r}''}{\mathbf{r}'^2} - \frac{(\mathbf{r}' \cdot \mathbf{r}'')}{\|\mathbf{r}'\|^4}\mathbf{r}'\right) \\ 0 \end{bmatrix} + \begin{bmatrix} GI_p K\left(\frac{\mathbf{r}' \times \mathbf{r}''}{\|\mathbf{r}'\|^3}\right) \\ \mathbf{0}_{3\times 1} \\ GI_p K \end{bmatrix} \tag{20}$$

Moreover, inserting Eq. (10) into $\delta\boldsymbol{\Upsilon} \cdot (\boldsymbol{\lambda} + p\boldsymbol{\Upsilon})$ allows one to write the weak form of virtual works (denoted $\mathcal{G}$ in what follows) as

$$\mathcal{G} = \int_0^1 \begin{bmatrix} \delta\mathbf{r} \\ \delta\mathbf{r}' \\ \delta\theta \end{bmatrix} \cdot (\mathbf{f}_{\text{dyn}} - \mathbf{f}_g - \mathbf{f}_{\text{ext}}) + \begin{bmatrix} \delta\mathbf{r}' \\ \delta\mathbf{r}'' \\ \delta\theta' \end{bmatrix} \cdot \mathbf{f}_{\text{stat}} dX + \begin{bmatrix} \delta\mathbf{r}(0) \\ \delta\mathbf{r}'(0) \\ \delta\theta(0) \end{bmatrix} \cdot \mathbf{f}_c(t,0) + \begin{bmatrix} \delta\mathbf{r}(1) \\ \delta\mathbf{r}'(1) \\ \delta\theta(1) \end{bmatrix} \cdot \mathbf{f}_c(t,1) + \delta\boldsymbol{\lambda} \cdot \boldsymbol{\Upsilon} = 0 \tag{21}$$

where $\mathbf{f}_c(t,0)$ and $\mathbf{f}_c(t,1)$ are given by

$$\mathbf{f}_c(t,X) = \begin{bmatrix} \boldsymbol{\lambda}_{\mathbf{r}} + p(\mathbf{r} - \mathbf{r}_d(t,X)) \\ \boldsymbol{\lambda}_{\mathbf{r}'} + (\lambda_\vartheta + p(\vartheta - \vartheta_d(t,X)))\mathbf{u}_n(X) + p(\mathbf{r}' - \mathbf{r}'_d(t,X)) \\ \lambda_\vartheta + p(\vartheta - \vartheta_d(t,X)) \end{bmatrix} \tag{22}$$

4 Principle of the Numerical Algorithm

At this point, the dynamic problem turns into a variational problem, which consists in finding at each time t, the fields $\mathbf{R}$, $\mathbf{r}$, $\dot{\mathbf{r}}$, $\ddot{\mathbf{r}}$, and $\boldsymbol{\lambda}$, satisfying Eq. (21) for any $\delta\boldsymbol{\Phi}$ and $\delta\boldsymbol{\lambda}$ imposed on the cable. The numerical algorithm proposed to solve this problem is based on a Newmark time integrator coupled to a Newton algorithm [31]. Moreover, due to the Euler–Bernoulli assumption, only the position field $\mathbf{r}$ is concerned by the time integration, the torsion state being governed by the static equilibrium. This has two important consequences on the following: first, the "roll dynamics" can be interpreted as infinitely fast (in the sense of the "singular perturbation theory") and, second, the roll dynamics will present some singularities when the boundary conditions at both ends of the cable are free. Fortunately, this case is not relevant for standard applications (see the examples at the end of this article). Whatever the case, if the cable is free at both ends, it is necessary to invoke a more refined model, such as that of Rayleigh [23] or Reissner [6] (if the length/thickness ratio is not too high), which both take into account the rotational kinetic energy of cross section, and so removing the eventual roll singularities. However, these two models require the development of a time integrator on

[4] In fact, one of the two integrations by parts is done; the second will be "replaced" by the polynomial interpolation (Hermit) of the finite element method.

the curved manifolds $SO(3)$ [32] or $S^2\times SO(2)$ [23] or, alternatively, the introduction of a vector parameterization of finite rotation [7] so compromising the simplicity of the geometrically exact approach. In our case, since the field $\mathbf{r}$ evolves in a vector space, the time integration has been readily achieved through the Newmark algorithm, which is quite standard for structural dynamics. In particular, no special work has been performed here to enhance energy and momentum conservation properties of the time integration.

In order to apply the Newton algorithm between two time steps, we have to compute the Jacobian of the resulting algebraic nonlinear problem. This is achieved, thanks to the linearization of the weak form Eq. (21) under the constraints imposed by the Newmark integration scheme. First of all, let us note that these constraints force the velocity and acceleration increment constructed on two steps of the Newton algorithm to verify

$$\Delta\dot{\mathbf{r}}(t,.)=\frac{\gamma}{\beta\Delta t}\Delta\mathbf{r}(t,.),\quad \Delta\ddot{\mathbf{r}}(t,.)=\frac{1}{\beta\Delta t^2}\Delta\mathbf{r}(t,.) \tag{23}$$

where, for any field f, we use the notation $\Delta f(t,.)=f^{(k)}(t,.)-f^{(k-1)}(t,.)$, with $f^{(k)}$ denoting the field computed at the kth Newton iteration. Then, the linearized weak form required by the Newton algorithm is computed by applying the operator "second variation" denoted by Δ to Eq. (21) (see Ref. [33]). Finally, we obtain

$$\begin{aligned}\Delta\mathcal{G}=&\int_0^1\begin{bmatrix}\delta\mathbf{r}\\ \delta\mathbf{r}'\\ \delta\theta\end{bmatrix}\cdot(\Delta\mathbf{f}_{\text{dyn}}-\Delta\mathbf{f}_g-\Delta\mathbf{f}_{\text{ext}})+\begin{bmatrix}\delta\mathbf{r}'\\ \delta\mathbf{r}''\\ \delta\theta'\end{bmatrix}\cdot\Delta\mathbf{f}_{\text{stat}}dX\\ &+\begin{bmatrix}\delta\mathbf{r}(0)\\ \delta\mathbf{r}'(0)\\ \delta\theta(0)\end{bmatrix}\cdot\Delta\mathbf{f}_c(t,0)+\begin{bmatrix}\delta\mathbf{r}(1)\\ \delta\mathbf{r}'(1)\\ \delta\theta(1)\end{bmatrix}\cdot\Delta\mathbf{f}_c(t,1)+\delta\boldsymbol{\lambda}\cdot\Delta\boldsymbol{\Upsilon}=0\end{aligned} \tag{24}$$

where we make the second variations appear (produced by $\Delta\Phi=(\Delta\mathbf{r},\Delta\mathbf{R})$, with $\Delta\mathbf{R}=(\Delta\theta\mathbf{t}_1+\mathbf{t}_1\times\Delta\mathbf{t}_1)\hat{}\,\mathbf{R}$, i.e., by an infinitesimal transformation compatible with Kirchhoff kinematics)

$$\Delta\mathbf{f}_{\text{dyn}}=\begin{bmatrix}\rho A\Delta\ddot{\mathbf{r}}\\ \mathbf{0}_{3\times1}\\ 0\end{bmatrix},\quad \Delta\mathbf{f}_g=\mathbf{0}_{7\times1},\quad \Delta\mathbf{f}_{\text{ext}}=\mathbf{K}_{\text{ext}}\begin{bmatrix}\Delta\mathbf{r}\\ \Delta\mathbf{r}'\\ \Delta\theta\end{bmatrix},$$

$$\Delta\mathbf{f}_{\text{stat}}=\mathbf{K}_{\text{stat}}\begin{bmatrix}\Delta\mathbf{r}'\\ \Delta\mathbf{r}''\\ \Delta\theta'\end{bmatrix}$$

$$\Delta\mathbf{f}_c(t,X)=\mathbf{K}_c(t,X)\begin{bmatrix}\Delta\mathbf{r}(X)\\ \Delta\mathbf{r}'(X)\\ \Delta\theta(X)\end{bmatrix}+\delta\boldsymbol{\Upsilon}_X\cdot\Delta\boldsymbol{\lambda}(X) \tag{25}$$

Furthermore, we introduce in Eq. (25) the tangent stiffness operators of external, internal, and constraint forces denoted by $\mathbf{K}_{\text{ext}}$, $\mathbf{K}_{\text{stat}}$, and $\mathbf{K}_c$, respectively, and detailed in Appendices A and B. Then, identifying the second variations $\Delta\dot{\mathbf{r}}$ and $\Delta\ddot{\mathbf{r}}$ with the Newton increment Eq. (23) allows one to rewrite the tangent dynamics Eq. (24) as

$$\begin{aligned}\Delta\mathcal{G}=&\int_0^1\begin{bmatrix}\delta\mathbf{r}\\ \delta\mathbf{r}'\\ \delta\theta\end{bmatrix}\cdot\left((\mathbf{K}_{\text{dyn}}-\mathbf{K}_{\text{ext}})\begin{bmatrix}\Delta\mathbf{r}(X)\\ \Delta\mathbf{r}'(X)\\ \Delta\theta(X)\end{bmatrix}\right)\\ &+\begin{bmatrix}\delta\mathbf{r}'\\ \delta\mathbf{r}''\\ \delta\theta'\end{bmatrix}\cdot\left(\mathbf{K}_{\text{stat}}\begin{bmatrix}\Delta\mathbf{r}'(X)\\ \Delta\mathbf{r}''(X)\\ \Delta\theta'(X)\end{bmatrix}\right)dX+\begin{bmatrix}\delta\mathbf{r}(0)\\ \delta\mathbf{r}'(0)\\ \delta\theta(0)\end{bmatrix}\cdot\left(\mathbf{K}_c(t,0)\right.\\ &\left.\times\begin{bmatrix}\Delta\mathbf{r}(0)\\ \Delta\mathbf{r}'(0)\\ \Delta\theta(0)\end{bmatrix}\right)+\begin{bmatrix}\delta\mathbf{r}(1)\\ \delta\mathbf{r}'(1)\\ \delta\theta(1)\end{bmatrix}\cdot\left(\mathbf{K}_c(t,1)\begin{bmatrix}\Delta\mathbf{r}(1)\\ \Delta\mathbf{r}'(1)\\ \Delta\theta(1)\end{bmatrix}\right)+\delta\boldsymbol{\Upsilon}\cdot\Delta\boldsymbol{\lambda}\\ &+\Delta\boldsymbol{\Upsilon}\cdot\delta\boldsymbol{\lambda}=0\end{aligned} \tag{26}$$

where $\mathbf{K}_{\text{dyn}}$ is the dynamic tangent stiffness operator given in Appendix A, whereas the last two constraint terms will be detailed in Sec. 5.

5 Finite Element Method

We now have all the ingredients required by the finite element resolution. For that, let us discretize the weak form Eq. (21) and its linearization Eq. (26) as follows. The beam of initial length $l=1$ is first of all subdivided into P elements subscripted e. Each element has a length l_e and a first point X_e (going along the beam from $X=0$ to l).

$$[0,1]=\bigcup_{e=1}^{P}[X_e,X_e+l_e] \tag{27}$$

The first and second variations of the position field $\mathbf{r}$ are interpolated using Hermit polynomials while the first and second variations of the (iterative) roll angle $(\delta\theta,\Delta\theta)$ are interpolated using Lagrange ones, i.e., for any $X\in[X_e,X_e+l_e]$

$$\begin{aligned}\delta\mathbf{r}(X)=&N_{I,e}(X)\,\delta\mathbf{r}_{I,e}+M_{I,e}(X)\,\delta\mathbf{r}'_{I,e},\quad \Delta\mathbf{r}(X)=N_{I,e}(X)\Delta\mathbf{r}_{I,e}\\ &+M_{I,e}(X)\Delta\mathbf{r}'_{I,e}\\ \delta\theta(X)=&L_{I,e}(X)\,\delta\theta_{I,e},\quad \Delta\theta(X)=L_{I,e}(X)\Delta\theta_{I,e}\end{aligned} \tag{28}$$

where (N_I,M_I) and L_I are the Hermit and Lagrange polynomials, respectively. Note that the summation convention on repeated subscripts $(I=1,2)$ is adopted. Finally, considering the partition Eq. (27) and inserting Eq. (28) in Eqs. (21) and (26) give the discrete equilibrium and its discrete linearization (a tilde symbol denotes a discrete vector coming from a continuous field)

$$\widetilde{\mathcal{G}}=(\delta\mathbf{q}^T,\delta\boldsymbol{\lambda}^T)\begin{bmatrix}\widetilde{\mathbf{f}}_{\text{dyn}}+\widetilde{\mathbf{f}}_{\text{stat}}-\widetilde{\mathbf{f}}_{\text{ext}}+\widetilde{\mathbf{f}}_c\\ \boldsymbol{\Upsilon}\end{bmatrix}=(\delta\mathbf{q}^T,\delta\boldsymbol{\lambda}^T)\widetilde{\mathbf{r}}_+=0 \tag{29}$$

and

$$\begin{aligned}\Delta\widetilde{\mathcal{G}}=&(\delta\mathbf{q}^T,\delta\boldsymbol{\lambda}^T)\begin{bmatrix}\widetilde{\mathbf{K}}_{\text{dyn}}+\widetilde{\mathbf{K}}_{\text{stat}}-\widetilde{\mathbf{K}}_{\text{ext}}+\widetilde{\mathbf{K}}_c & \widetilde{\mathbf{J}}^T\\ \widetilde{\mathbf{J}} & 0\end{bmatrix}\begin{bmatrix}\Delta\mathbf{q}\\ \Delta\boldsymbol{\lambda}\end{bmatrix}\\ =&(\delta\mathbf{q}^T,\delta\boldsymbol{\lambda}^T)\widetilde{\mathbf{K}}_+\begin{bmatrix}\Delta\mathbf{q}\\ \Delta\boldsymbol{\lambda}\end{bmatrix}=0\end{aligned} \tag{30}$$

where $\delta\mathbf{q}$ and $\Delta\mathbf{q}$ are the $7(P+1)\times1$ vectors of nodal variations appearing in Eq. (28) while $\widetilde{\mathbf{f}}_{\text{dyn}}$, $\widetilde{\mathbf{f}}_{\text{stat}}$, and $\widetilde{\mathbf{f}}_{\text{ext}}$ and $\widetilde{\mathbf{K}}_{\text{dyn}}$, $\widetilde{\mathbf{K}}_{\text{stat}}$, and $\widetilde{\mathbf{K}}_{\text{ext}}$ are $7(P+1)\times1$ force vectors and $7(P+1)\times7(P+1)$ band matrices, respectively, obtained by assembling the corresponding elementary forces and stiffness matrices. On the other hand, the constraint forces and stiffness do not require any assembling procedure since we simply have $\widetilde{\mathbf{f}}_c=(\mathbf{f}_c^T(t,0),\mathbf{0}_{1\times7(P-1)},\mathbf{f}_c^T(t,1))^T$ and $\widetilde{\mathbf{K}}_c=\text{diag}_{e=1,\ldots,P+1}(\mathbf{K}_{c,e})$, with $\mathbf{K}_{c,e}=\mathbf{0}_{7\times7}$, except $\mathbf{K}_{c,1}=\mathbf{K}_c(t,0)$ and $\mathbf{K}_{c,P+1}=\mathbf{K}_c(t,1)$. Finally, due to the discretization of $\delta\boldsymbol{\Upsilon}\Delta\boldsymbol{\lambda}$

$+\Delta\mathbf{Y}\,\delta\boldsymbol{\lambda}$, we also introduce the $14\times 7(P+1)$ matrix $\widetilde{\mathbf{J}}$ given by

$$\widetilde{\mathbf{J}}=\begin{bmatrix}\mathbf{J}(0) & \mathbf{0}_{7\times 7P}\\ \mathbf{0}_{7\times 7P} & \mathbf{J}(1)\end{bmatrix},\quad \text{with } \mathbf{J}(X)=\begin{bmatrix}\mathbf{I}_3 & \mathbf{0}_{3\times 3} & \mathbf{0}_{3\times 1}\\ \mathbf{0}_{3\times 3} & \mathbf{I}_3 & \mathbf{0}_{3\times 1}\\ \mathbf{0}_{1\times 3} & \mathbf{u}_n^T(X) & 1\end{bmatrix} \tag{31}$$

as well as the augmented residue vector and stiffness matrix denoted by $\widetilde{\mathbf{r}}_+$ and $\widetilde{\mathbf{K}}_+$, respectively. Finally, once discretized, the linear expansion of the equilibrium at $t+\Delta t$ gives the linear discrete system

$$\widetilde{\mathbf{K}}^{(k)}_{+_{(t+\Delta t)}}\Delta\mathbf{q}^{(k+1)}_{(t+\Delta t)}=-\,\widetilde{\mathbf{r}}^{(k)}_{+_{(t+\Delta t)}} \tag{32}$$

that we solve at each Newton step k with respect to the vector of nodal increments $\Delta\mathbf{q}^{(k+1)}_{t+\Delta t}$.

6 Updating Formulae

In order to solve the balance equilibrium, it is necessary to update the forces and the tangent stiffness operators at each Newton iteration k. This is achieved by updating the position, tangent, and curvature fields $\mathbf{r}$, $\mathbf{r}'$, and $\mathbf{r}''$, the velocity and acceleration fields $\dot{\mathbf{r}}$ and $\ddot{\mathbf{r}}$, the torsion rate field K, the roll angles at the two boundaries $\vartheta(0)$ and $\vartheta(1)$, as well as the associated vectors of Lagrange multipliers $\boldsymbol{\lambda}(0)$ and $\boldsymbol{\lambda}(1)$. We give below the updating formulae of these fields, at any point $X\in[X_e,X_e+l_e]$. To be used, these formulae first require Eq. (32) to be solved with respect to the vector of nodal increments $\Delta\mathbf{q}^{(k+1)}_{(t+\Delta t)}$ and second, Eq. (28) to be invoked to get the current incremental fields that we simply note $\Delta\mathbf{r}$, $\Delta\mathbf{r}'$, and $\Delta\mathbf{r}''$. These are the following.

1. Updating of the position, tangent, and curvature fields
$$\mathbf{r}^{(k+1)}_{(t+\Delta t)}=\mathbf{r}^{(k)}_{(t+\Delta t)}+\Delta\mathbf{r},\quad \mathbf{r}'^{(k+1)}_{(t+\Delta t)}=\mathbf{r}'^{(k)}_{(t+\Delta t)}+\Delta\mathbf{r}',\quad \mathbf{r}''^{(k+1)}_{(t+\Delta t)}=\mathbf{r}''^{(k)}_{(t+\Delta t)}+\Delta\mathbf{r}''$$
2. Updating of the velocity and acceleration fields
$$\dot{\mathbf{r}}^{(k+1)}_{(t+\Delta t)}=\dot{\mathbf{r}}^{(k)}_{(t+\Delta t)}+\frac{\gamma}{\beta\Delta t}\Delta\mathbf{r},\quad \ddot{\mathbf{r}}^{(k+1)}_{(t+\Delta t)}=\ddot{\mathbf{r}}^{(k)}_{(t+\Delta t)}+\frac{1}{\beta(\Delta t)^2}\Delta\mathbf{r}$$
The following field is not explicitly required by the formulation; nevertheless, it is of practical interest since it intervenes as an intermediate variable in many calculations.
3. Updating of the unit tangent field
$$\mathbf{t}^{(k+1)}_{1,(t+\Delta t)}(X)=\frac{\mathbf{r}'^{(k+1)}_{(t+\Delta t)}(X)}{\|\mathbf{r}'^{(k+1)}_{(t+\Delta t)}(X)\|}$$
4. Updating of the orientation field. Replacing the two arbitrary configurations of Eq. (1), by two successive configurations of the Newton algorithm, the updating of the rotation field is done as follows:
$$\mathbf{R}^{(k+1)}_{(t+\Delta t)}=\exp(\Delta\theta(\mathbf{t}_1+\Delta\mathbf{t}_1)\hat{}\,)\boldsymbol{\Lambda}_{\mathbf{t}_1}(\mathbf{t}_1+\Delta\mathbf{t}_1)\mathbf{R}^{(k)}_{(t+\Delta t)} \tag{33}$$
with
$$\mathbf{t}_1=\mathbf{t}^{(k)}_{1,(t+\Delta t)}(X),\quad \Delta\mathbf{t}_1=\mathbf{t}^{(k+1)}_{1,(t+\Delta t)}(X)-\mathbf{t}^{(k)}_{1,(t+\Delta t)}(X),$$
$$\Delta\theta=\Delta\widetilde{\theta}^{(k)}_{(t+\Delta t)}(X)$$
5. Updating of the torsion rate. The updating formula of K results from the answer to the following question: "What is the finite increment ΔK generated by a finite variation of the configuration defined by $\Delta\mathbf{r}$ and $\Delta\theta$?" To get this result, we can, for instance, apply the Frenet formulae $K=\mathbf{t}_2'\cdot\mathbf{t}_3=-\mathbf{t}_3'\cdot\mathbf{t}_2$ to the updated configuration of the beam, and obtain after computations
$$K^{(k+1)}_{(t+\Delta t)}=K^{(k)}_{(t+\Delta t)}-\frac{1}{1+\mathbf{t}^{(k)}_{1,(t+\Delta t)}\cdot\mathbf{t}^{(k+1)}_{1,(t+\Delta t)}}[((\mathbf{t}^{(k+1)}_{1,(t+\Delta t)}\times\mathbf{t}'^{(k+1)}_{1,(t+\Delta t)})\cdot\mathbf{t}^{(k)}_{1,(t+\Delta t)})-(\mathbf{t}^{(k)}_{1,(t+\Delta t)}\times\mathbf{t}'^{(k)}_{1,(t+\Delta t)})\cdot\mathbf{t}^{(k+1)}_{1,(t+\Delta t)}]+\Delta\theta'$$
6. Updating of the roll angle. After having updated the rotation field as in Eq. (33), we can extract from it the new incremental roll angle ϑ at any point of the beam. This is achieved by inverting the identity Eq. (3), where the current configuration here is the $(k+1)$th configuration calculated by the Newton algorithm
$$\vartheta^{(k+1)}_{(t+\Delta t)}=\exp^{-1}_{\hat{\mathbf{t}}^{(k+1)}_{(t+\Delta t)}}(\boldsymbol{\Lambda}^T_{\mathbf{t}_{1n}}(\mathbf{t}^{(k+1)}_{1_{(t+\Delta t)}})\mathbf{R}^T_n\mathbf{R}^{(k+1)}_{(t+\Delta t)})$$
where we introduce the inverse map $\exp^{-1}_{\hat{\mathbf{V}}}$ such that $\exp^{-1}_{\hat{\mathbf{V}}}(\exp(\alpha\hat{\mathbf{V}}))=\alpha\in[0,2\pi]$.
7. Updating of the Lagrange multipliers. Because they belong to a linear space, the Lagrange multipliers are updated by the simple additive formula
$$\boldsymbol{\lambda}^{(k+1)}_{(t+\Delta t)}=\boldsymbol{\lambda}^{(k)}_{(t+\Delta t)}+\Delta\boldsymbol{\lambda}^{(k+1)}_{(t+\Delta t)},\quad \text{with } \boldsymbol{\lambda}^{(0)}_{(t+\Delta t)}=0$$

7 Numerical Illustrations

In what follows, the previous model is illustrated on three cases related to robotics and fluid-structure interaction fields. Due to weak instabilities introduced by the algebraic constraints in the first case and in order to reach a stable FSI coupling while keeping standard time step in the second, a modified version of the Newmark time scheme has to be used for the structural solver such as the Hilber-Hughes-Taylor (HHT) [34], the Bossak [35] method, or the α-generalized technique [36]. These algorithms introduce a numerical dissipation of the higher frequencies without degrading the accuracy. In the following results, the Bossak scheme was used with an α coefficient fixed to 0.1.

7.1 Robotics Application: Cable and Six-Axis Puma Robot. In the robotics field, cables or flexible tubes are found everywhere since they bring electric or hydraulic power to the actuators. The main problems are how to guide them, how to avoid collisions, and how to minimize their wear. The present illustrations will show that the beam solver can predict the movement and positions of a complex robotics problem.

We consider a six degrees of freedom (DOFs) manipulator of the Puma type (cf. Fig. 3). The time evolution of the joints is defined in Table 1. The cable is clamped to the robot at the origin of the tool frame O_7, and to the earth at the point C of the environment. Its characteristics are presented in Table 2. Figure 3 shows the robot and the cable in the initial configuration of the motion. The initial configuration of the cable is deduced from a vertical straight reference configuration by applying the constraint Eq. (5) to it with an imposed motion compatible with its manipulation by a person. This preliminary mounting phase first considers the cable embedded in C and lying under gravity. Then, the free end of the cable is brought along the circular α-parameterized path defined in Table 3 until it reaches the point O_7 while the robot is in the initial configuration of Fig. 3.

Once the mounting phase has been achieved, the tool begins to move at $t=0$, according to the imposed motion of the robot (Table 1). The time-varying constraints (see Eq. (5)) imposed on the moving end of the cable are deduced from the direct geometric model of the Puma type manipulator with Denavit–Hartenberg parameters [37] $r_1=d_4=1$ m and $r_5=r_7=0.3$ m. The spatial discretization uses ten finite elements. The mounting phase is first performed using a static version of the algorithm. Then, the simulation is achieved over a duration of 4 s with a time step of $\Delta t=0.001$ s. Figure 4, which shows snapshots at every 25 ms, highlights the dynamic effects such as the pendular oscillations due to

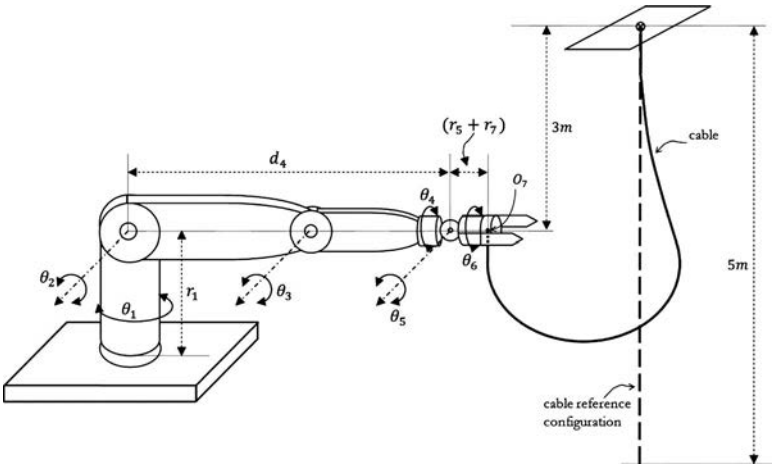

Fig. 3 Initial configuration of the six-axis "Puma robot"

gravity and the high velocity of the robot.

Table 4 shows the typical evolution of the residual vector norm during the iterations of the beam solver for one time step (the convergence for the others is quite similar).

Today, this solver is in progress toward virtual reality and haptic applications. In this case, it becomes necessary to address the problem of collision modeling, which is not considered here.

7.2 2D FSI Illustration: Hübner Test-Case. Another application, where this model is relevant, concerns risers used in oceanic engineering. In this case, FSI is involved. Thus, the previous cable model has to be coupled with a fluid solver. As a first step toward this goal, we consider here the benchmark due to Hübner. This FSI application was originally carried out by Wall and Ramm [38] in order to demonstrate the ability of their FSI formulation to deal with complex flow-flexible structure interactions exhibiting large deformations. In 2004, Huebner et al. modified the inflow velocity and used this new problem to test his monolithic code [39].

The application consists of a thin elastic nonlinear beam attached to a fixed square rigid body, plunged in an incompressible fluid flow (cf. Fig. 5). The square rigid body produces a very unsteady phenomenon: Vortices separate alternatively from its corners. These vortices create an oscillating force on the filament, which deforms itself.

The fluid and structure characteristics are given in Table 5. The Reynolds number is fixed to 204; the computation is consequently done with a laminar flow. The boundary conditions are set to the following:

1. imposed velocity at the inflow, upper, and lower boundaries
2. imposed pressure at the outflow
3. adherence boundary on the filament

Two meshes are generated using the commercial software GRIDGEN™. One is totally unstructured and coarse ($\simeq$4000 cells and $\simeq$2000 nodes). The second is finer ($\simeq$33,000 cells and $\simeq$27,000 nodes) and it is structured near the body and then fully unstructured.

Flows are computed using an in-house solver ISIS-CFD, developed by the Equipe Modélisation Numérique (EMN) of the Fluid Mechanics Laboratory of the Ecole Centrale Nantes. It solves the incompressible unsteady Reynolds-averaged Navier–Stokes (RANS) equations under isothermal conditions on generalized unstructured meshes, enabling complex geometries to be dealt with. The solver is based on a finite-volume method to build a second-order accurate discretization of the RANS equations. An arbitrary Lagrangian Eulerian (ALE) approach is used to deal with moving bodies. Ad-hoc deformation techniques have thus been developed to keep a body-fitted mesh during its motion.

At first, the filament is supposed to be rigid and only a fluid problem is solved. The flow is then established after 8 s and a Fourier analysis is performed on the lift effort: The dominant frequency of the fluid field yields $f_1^f = 3.74$ Hz, which is in good agreement with the Hübner result [39].

Now, the filament is considered as a deformable beam. In principle, the physics of the FSI problem is the following: The beam is

Table 1 Joint time evolutions

j	θ_j	ω_j
1	$\theta_1(t) = \pi/6 \sin(\omega_1 t)$	$\omega_1 = \pi$
2	0	0
3	0	0
4	$\theta_4(t) = -\pi/2 + \pi/6 \sin(\omega_4)$	$\omega_1 = \pi$
5	$\theta_5(t) = \pi/6 \sin(\omega_5 t)$	$\omega_5 = \pi$
6	0	0
7	0	0

Table 2 Cable characteristics (SI units)

Length	$L = 5$ m
Diameter	$d = 0.015$ m
Lineic mass	$\mu = 5$ kg m^{-1}
Stretching stiffness	$EA = 5 \times 10^7$ N
Twisting stiffness	$GI_p = 9 \times 10^2$ N.m^2
Bending stiffness	$EI_a = 5 \times 10^2$ N.m^2

Table 3 Imposed motions during the mounting phase (SI units)

Imposed motions in $X = 0$	Imposed motions in $X = L$
$\mathbf{r}_d^T(0) = (0,0,0)$	$\mathbf{r}_d^T(L) = ((L-2) + 2/\alpha \sin(\alpha), -2/\alpha + 2/\alpha \cos(\alpha), 0),\ \alpha \in [0, \pi]$
$\mathbf{r}_d'^T(0) = (1,0,0)$	$\mathbf{r}_d'^T(L) = (\cos(\alpha), -\sin(\alpha), 0),\ \alpha \in [0, \pi]$
$\vartheta_d(0) = 0$	$\vartheta_d(L) = 0$

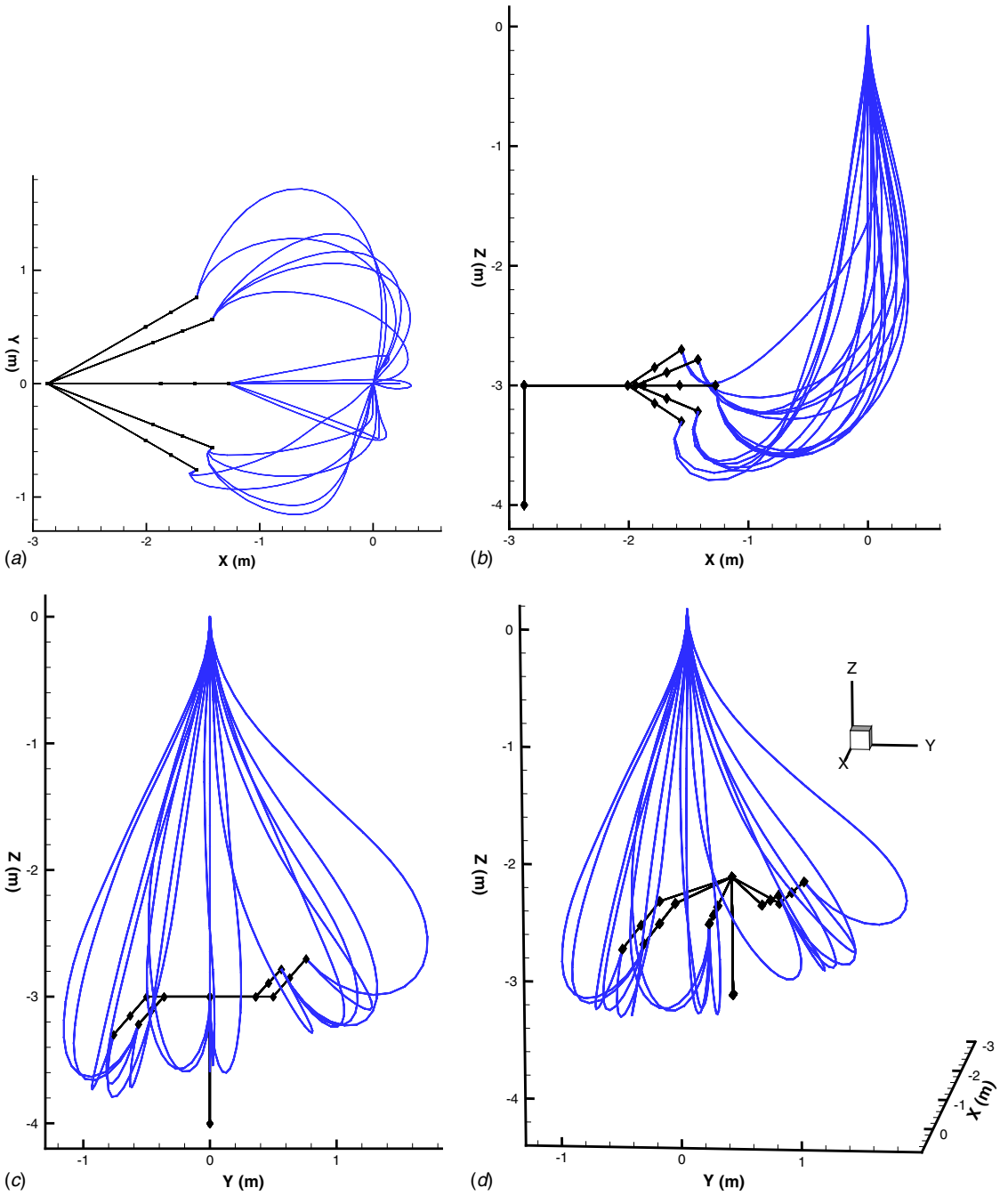

Fig. 4 A cable fixed at the end of a moving Puma type manipulator: (*a*) planar projection in $(\mathbf{e}_1,\mathbf{e}_2)$, (*b*) planar projection in $(\mathbf{e}_3,\mathbf{e}_1)$, (*c*) planar projection in $(\mathbf{e}_2,\mathbf{e}_3)$, and (*d*) 3D visualization

submitted to the hydrodynamic (viscous and pressure) forces exerted by the fluid through its boundaries. These forces make the beam move. As a feedback, the motion of the beam modifies the boundary conditions of the flow, so closing the chain of causalities (see Fig. 6).

To handle this problem numerically, the CFD solver is coupled with the geometrically exact beam solver presented here. More precisely, an implicit/iterative algorithm (see Fig. 7) is used to coordinate the data exchanges between the fluid and solid solvers and obtain a stable coupling [40]. This algorithm is structured into three hierarchical loops. The highest level corresponds to the temporal loop. The second one, denoted here as the FSI loop, aims to solve the nonlinearities of the fluid problem. Included in it, the third loop calls the beam solver. Thus, at each new FSI iteration (where the time is fixed), the structure problem is solved until convergence on the geometric nonlinearities using the current fluid loads (beam loop). It can be done at each FSI iteration since the CPU time of the structure resolution is negligible compared with that of the fluid resolution. The computed configuration of the beam is then updated. In particular, an adjustment of the fluid mesh is carried out to fit with the updated configuration of the beam. At that time, the core of the fluid solver is called to obtain

Table 4 Typical convergence history

Iteration	0	1	2	3
Residual	$1.2e6$	$1.0e3$	0.16	$4.6e-8$

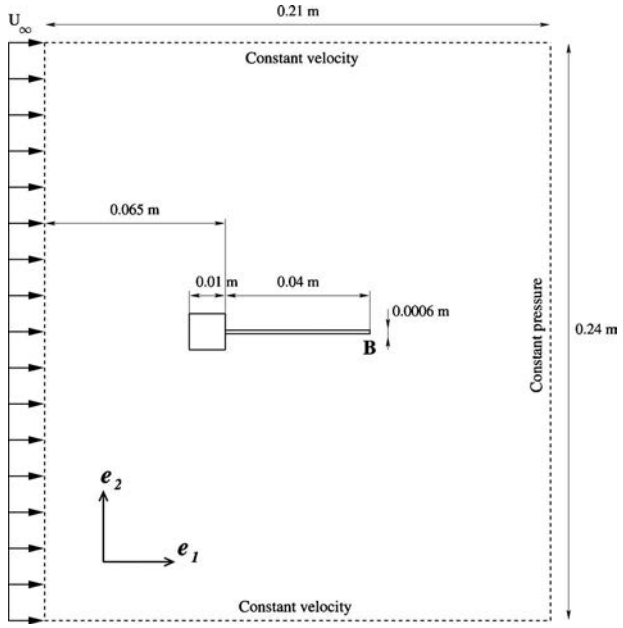

Fig. 5 Elastic filament fixed to a square rigid body in an incompressible flow

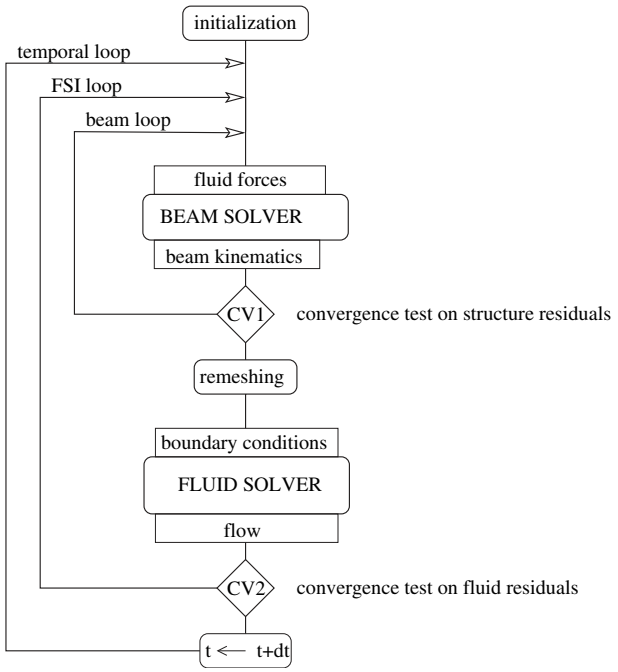

Fig. 7 Algorithm of the FSI coupling

a new computation of the current flow (inducing new values of fluid loads for the beam). A new nonlinear iteration can thus restart. This coupling process (FSI loop) is repeated until convergence of the fluid flow (since the beam structure is almost solved up to the zero machine each time). Then, a new time step can go on.

As an illustration, Table 6 shows the residual norm for the structure problem during the iterations of the beam solver (at a given fluid nonlinear iteration of a given time step).

One of the difficulties in fluid-structure interaction is due to the fact that the fluid and solid meshes do not generally match (cf. Ref. [41]). In the present case, the dimensions of the two media models are not even the same. In fact, from the structure point of view, the beam is represented by its discretized 1D centroidal line, whereas the fluid views the structure by a set of boundary faces around this line (see Fig. 8(*a*)). As a consequence, the 3D contact forces (pressure and viscous) exerted by the fluid on the boundaries of the beam have to be converted into a set of nodal wrenches compatible with Kirchhoff kinematics. The fluid forces acting on the beam are initially described by elementary forces applied on each face of the fluid mesh in contact with the beam boundary (Fig. 8(*b*)). Due to possible overlaps of fluid faces on beam elements, the faces are split on each element into a set of subfaces. Then, for each subface (which belongs to a single beam element), the corresponding part of the contact force is applied as a localized one at the geometric center of the subface (Fig. 8(*c*)). In the end, we have, on each beam element, a set of localized 3D loads exerted onto the wetted boundaries of some intermediate cross sections (between the two nodes of each element) (see Fig. 9(*a*)). Then, invoking Kirchhoff kinematics, these forces are first changed into localized generalized forces $\mathbf{f}_{\text{ext}}$ (Fig. 9(*b*)). Next, these forces are discretized and assembled into the vector $\widetilde{\mathbf{f}}_{\text{ext}}$ (of the form given by Eq. (19)), which is applied at the two end nodes of the beam by invoking the nodal interpolation (Fig. 9(*c*)). This process ensures the global conservation of the forces, which is an important criterion to fulfill. Finally, when computing $\widetilde{\mathbf{K}}_{\text{ext}}$, only the beam configuration dependence is taken into account in the linearization of $\mathbf{f}_{\text{ext}}$. Indeed, the complete computation of $\widetilde{\mathbf{K}}_{\text{ext}}$ would require the numerical Jacobian of the CFD solver to be computed, which is prohibitive (in terms of complexity and CPU time). This choice explains why we assumed the hydrodynamic wrench density (see Eq. (16)) to be of the follower type. Note that even if $\widetilde{\mathbf{f}}_{\text{ext}}$ is only considered as an imposed force (without computation $\widetilde{\mathbf{K}}_{\text{ext}}$), the FSI coupling is also successful.

Table 5 Hübner test-case characteristics (SI units)

Square edge	$a=0.01$ m
Beam length	$L=0.04$ m
Beam thickness	$d=0.0006$ m
Young modulus	$E=2$ MPa
Solid density	$\rho_s=2000$ kg m^{-3}
Fluid density	$\rho_f=1.18$ kg m^{-3}
Dynamic viscosity	$\mu_f=1.8210^{-5}$ Pa s
Inflow velocity	$U_\infty=0.315$ m s^{-1}

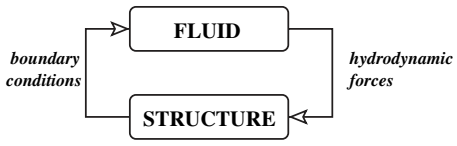

Fig. 6 Diagram of FSI coupling

In the Hübner problem with a deformable beam, the time step is set at $\Delta t=10^{-3}$ s. The inflow leads to the production of vortices and so the filament begins to oscillate in the second mode. Figure 10 represents the deflection of the free end of the beam y_B in time. This curve can be compared with the following results of Valdés Vázquez [42] and Hübner.

1. The free end evolution is very similar (the maximum amplitude is reached at 8×10^{-3} m).
2. The first oscillating frequency obtained by FFT around 3 Hz

Table 6 Typical convergence history of the beam solver

Iteration	0	1	2	3	4	5
Residual	4.22	2.8$e-2$	2.1$e-2$	1.1$e-4$	1.0$e-4$	5.3$e-7$

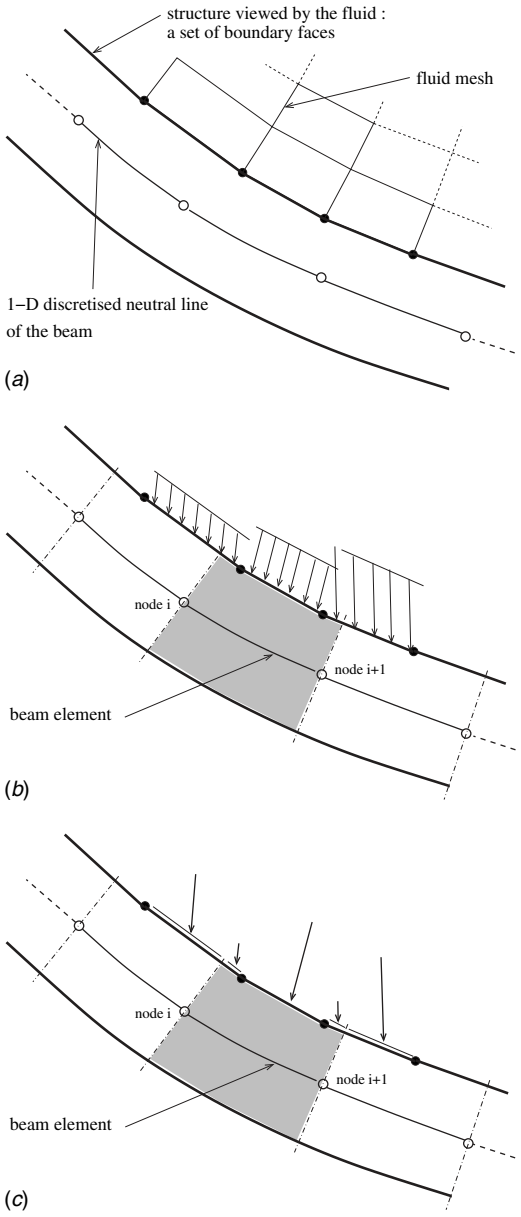

Fig. 8 Models of the structure and fluid loads

is in quite good agreement with the results of Valdés Vázquez and Hübner (3.22 Hz and 3.1 Hz, respectively).

The coupled problem frequency $f_1^c \approx 3$ Hz is similar to the dominant frequency of the fluid ($f_1^f = 3.74$ Hz) and the second natural frequency of the structural part ($f_2^s = 4.09$ Hz) but it is lower, and so we can think that the first frequency of the structure ($f_1^s = 0.61$ Hz) influences the coupled problem.

From the beam point of view, the results obtained with the coarse or fine fluid meshes are very similar. However, with the fine mesh, the details of the fluid flow are better described (cf. Fig. 11). The number of beam finite elements can be reduced from 100 to 20 without a noticeable degradation of the beam motion. Finally, we recover the good numerical performance of the geometrically exact approach since a limited number of elements leads to a grid-independent solution (as a comparison, 123 elements were used in Ref. [42]).

7.3 3D FSI Illustration: A Towed Cable in Water. A 3D IFS simple test-case has been done in order to show the capabilities of

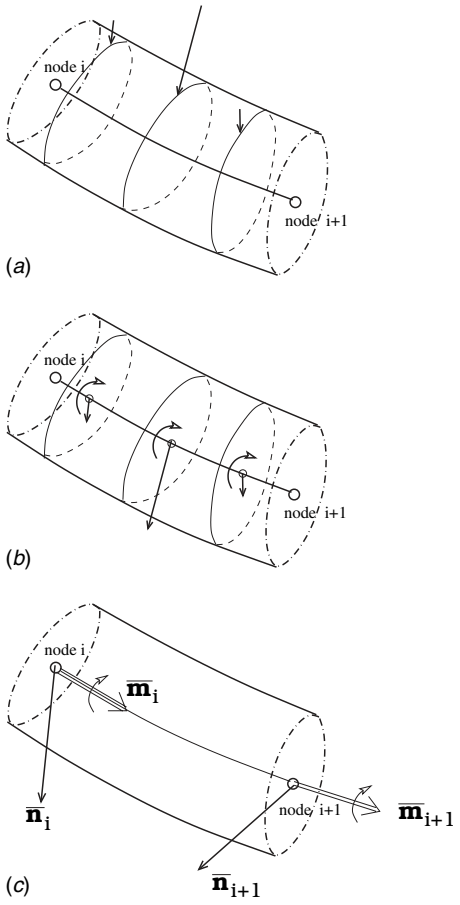

Fig. 9 Transfer of fluid contact forces to external wrenches compatible with Kirchhoff beam kinematics

the FSI code in 3D and to prepare the program to work on riser/ VIV problems: A deformable cable is fixed at an extremity, free at the other, and is partly dived into water (see Fig. 12). The following two different configurations were realized using the same coupling procedure described in Sec. 7.2:

1. one with a fixed cable in a fluid with constant velocity (see Fig. 13)
2. one with a towed cable in still water (see Fig. 14)

In both configurations, the cable deforms itself a lot (see Fig. 13) and periodically oscillates. It is a consequence of the VIV. The position of nodes is updated using the same grid deformation technique used for the Hübner test-case 7.2 to recover a body-fitted mesh each time it is needed. Near the body, the cells are not deformed and, so, are always orthogonal to the cable (see Fig. 15), which is good for the quality of the results.

The two configurations are physically identical. However, the second one (where the cable is towed in still water (see Fig. 14) enables to use complex imposed motion at the cable extremity, for example, the cable could be slowly accelerated to reach the nominal velocity, which avoids a violent start).

8 Conclusion

In this article, we propose a geometrically exact finite element approach in order to solve the problem of nonlinear cable simulations in finite transformation with small strains. Two potential applications are envisaged by this work. The first is related to the prediction of motions and forces undergone by cables or other flexible pipes, which are often used in robotics for carrying energy to the actuators. The second concerns the interaction with a fluid

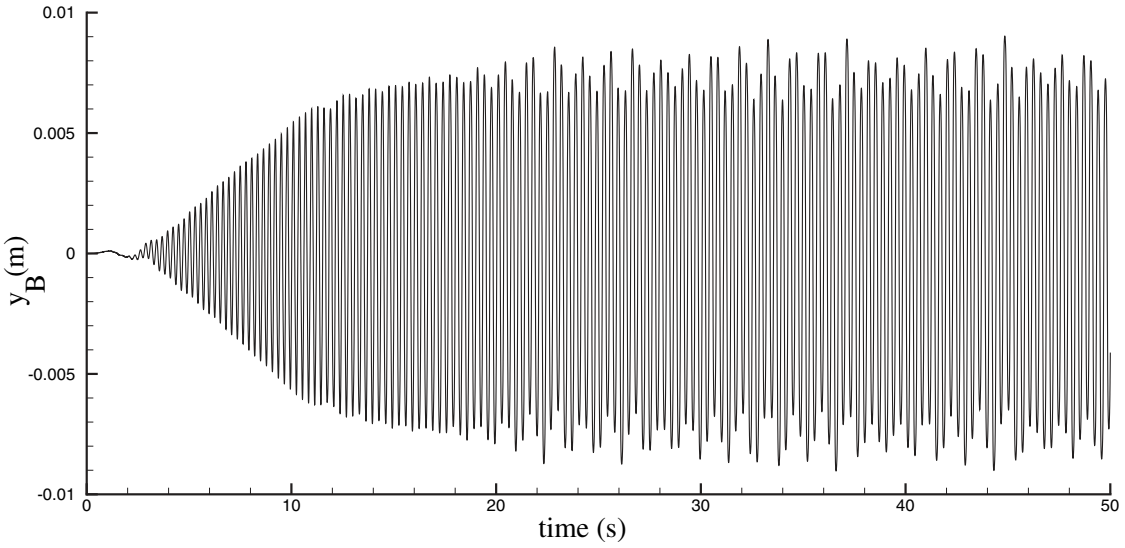

Fig. 10 Hübner test-case results with the Bossak method (Δt=10^{-3} s) on the coarse mesh

flow and especially the VIV phenomenon for undersea cables, such as risers, that are used in oceanic engineering or electric cables subjected to wind. As is usual when dealing with very elongated structures, such as ropes or cables, the model of the structure is that of Kirchhoff beams. However, the proposed finite element approach differs from the previous work on that topic by the fact that it is directly inspired by the geometrically exact approach initiated by Simo and his successors for dealing with Reissner–Timoshenko beams. In fact, like in this modeling framework, no approximation of the finite rotations is assumed in all the analytical computations required by the finite element method, except those related to the unavoidable time and space discretizations. Here, no advanced work has been investigated on this numerical part, and classical time integration has been used. Beyond these considerations, it will be useful to design specific time integrators able to preserve energy and momentum of the cable. This could be done through the growing results of geometric integrators [43–46], extending them to the configuration space $S^2 \times SO(2)$. Based on this nonlinear Euler–Bernoulli dynamic model, the problem of cable dynamics with imposed motions at the ends is investigated through an augmented Lagrangian approach. The resulting dynamic beam solver is also coupled with a CFD solver that deals with the Reynolds-averaged Navier–Stokes equations. The methodologies are presented here and validated through a 2D benchmark test-case of VIV. An illustration dealing with a 3D case is also shown. These results are currently being extended to more realistic 3D tests related to a riser, where experimental data are available. This integration opens the way to analyze more accurately FSI configurations with high Reynolds number turbulent flow around complex geometry. The challenge to simulate such configurations is vital in the industrial domain (such as off-shore). Finally, as regards its application to robotics, the solver is currently coupled with a numerical code devoted to the detection of collisions and the simulation of the contacts of the cable with itself and with its environment through nonsmooth dynamic techniques.

Appendix A: Dynamic and Internal Tangent Stiffness

Because only the stiffness operators are concerned in this Appendix, in what follows, all the fields subscripted by ϵ are deduced from those nonsubscripted by substituting the field $\mathbf{r}$ by its perturbation $\mathbf{r}_\epsilon = \mathbf{r} + \epsilon\Delta\mathbf{r}$ and the roll field ϑ by $\vartheta_\epsilon = \vartheta + \epsilon\Delta\vartheta$.

$$\mathbf{K}_{\text{dyn}} = \left.\frac{d}{d\epsilon}\right|_{\epsilon=0} \mathbf{f}_{\text{dyn},\epsilon} = \begin{bmatrix} \rho\dfrac{A}{\beta(\Delta t)^2}\mathbf{I}_3 & \mathbf{0}_{3\times3} & \mathbf{0}_{3\times1} \\ \mathbf{0}_{3\times3} & \mathbf{0}_{3\times3} & \mathbf{0}_{3\times1} \\ \mathbf{0}_{1\times3} & \mathbf{0}_{1\times3} & 0 \end{bmatrix}$$

$$\mathbf{K}_{\text{stat}} = \left.\frac{d}{d\epsilon}\right|_{\epsilon=0} \mathbf{f}_{\text{stat},\epsilon} = \begin{bmatrix} \mathbf{K}_{\text{stat},11} & \mathbf{K}_{\text{stat},12} & \mathbf{K}_{\text{stat},13} \\ \mathbf{K}_{\text{stat},21} & \mathbf{K}_{\text{stat},22} & \mathbf{0}_{3\times1} \\ \mathbf{K}_{\text{stat},31} & \mathbf{0}_{1\times3} & \mathbf{K}_{\text{stat},33} \end{bmatrix}$$

with

$$\mathbf{K}_{\text{stat},11} = EA\left[\left(1-\frac{1}{\|\mathbf{r}'\|}\right)\mathbf{I}_3 + \frac{1}{\|\mathbf{r}'\|^3}\mathbf{r}'\otimes\mathbf{r}'\right] + EI_a\left[-\frac{1}{\|\mathbf{r}'\|^4}(\|\mathbf{r}''\|^2\mathbf{I}_3 + \mathbf{r}''\otimes\mathbf{r}'') + \frac{4}{\|\mathbf{r}'\|^6}(\|\mathbf{r}'\|^2\mathbf{r}'\otimes\mathbf{r}' + (\mathbf{r}'\cdot\mathbf{r}'')(\mathbf{r}'\otimes\mathbf{r}'' + \mathbf{r}''\otimes\mathbf{r}')) + \frac{(\mathbf{r}'\cdot\mathbf{r}'')^2}{\|\mathbf{r}'\|^6}\left(2\mathbf{I}_3 - \frac{12}{\|\mathbf{r}'\|^2}\mathbf{r}'\otimes\mathbf{r}'\right)\right] + GI_p\left[-\frac{K}{\|\mathbf{r}'\|^3}\hat{\mathbf{r}}'' - 3\frac{K}{\|\mathbf{r}'\|^5}((\mathbf{r}'\times\mathbf{r}'')\otimes\mathbf{r}') + \frac{1}{\|\mathbf{r}'\|^6}(\mathbf{r}'\times\mathbf{r}'')\otimes(\mathbf{r}'\times\mathbf{r}'')\right]$$

$$\mathbf{K}_{\text{stat},11} = EI_a\left[\frac{1}{\|\mathbf{r}'\|^2}\mathbf{I}_3 - \frac{1}{\|\mathbf{r}'\|^4}\mathbf{r}'\otimes\mathbf{r}'\right]$$

$$\mathbf{K}_{\text{stat},21} = EI_a\left[-\frac{1}{\|\mathbf{r}'\|^4}(2\mathbf{r}''\otimes\mathbf{r}' + \mathbf{r}'\otimes\mathbf{r}'') - \frac{\mathbf{r}'\cdot\mathbf{r}''}{\|\mathbf{r}'\|^4}\mathbf{I}_3 + 4\frac{\mathbf{r}'\cdot\mathbf{r}''}{\|\mathbf{r}'\|^6}\mathbf{r}'\otimes\mathbf{r}'\right]$$

$$\mathbf{K}_{\text{stat},12} = \mathbf{K}_{\text{stat},21}^T + GI_p\left[\frac{K}{\|\mathbf{r}'\|^3}\hat{\mathbf{r}}'\right]$$

$$\mathbf{K}_{\text{stat},33} = GI_p$$

$$\mathbf{K}_{\text{stat},31} = GI_p\left[\frac{(\mathbf{r}'\times\mathbf{r}'')^T}{\|\mathbf{r}'\|^3}\right]$$

$$\mathbf{K}_{\text{stat},13} = \mathbf{K}_{\text{stat},31}^T$$

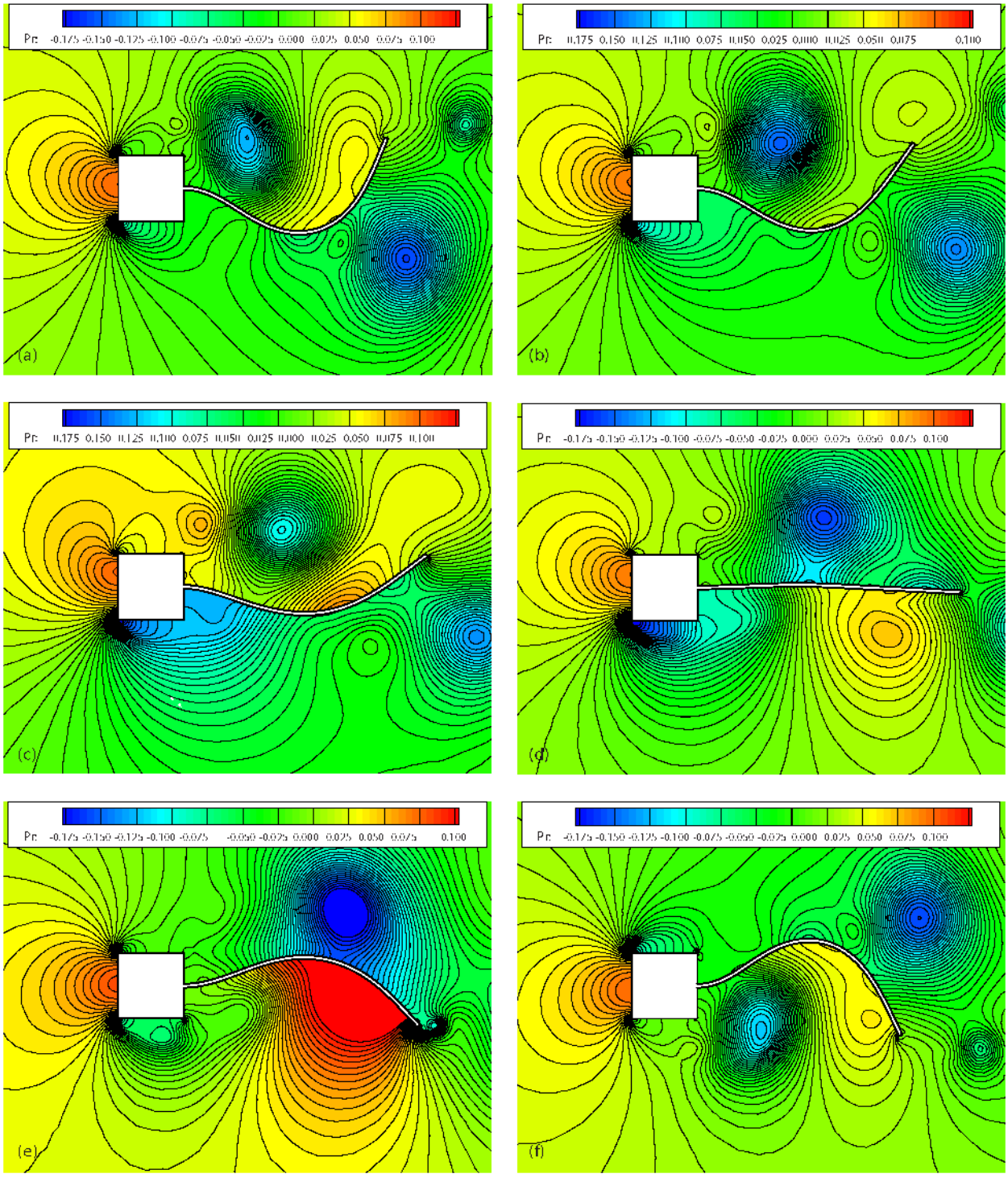

mesh) : (*a*) $t=0$, (*b*) $t\approx T/12$, (*c*) $t\approx T/6$, (*d*) $t\approx T/4$, (*e*) $t\approx T/3$, and (*f*) $t\approx T/2$

Appendix B: Tangent Stiffness of Follower Loads and Generalized Constraint Forces

Tangent stiffness of follower loads

$$\mathbf{K}_{\text{ext}} = \begin{bmatrix} \mathbf{0}_{3\times3} & \mathbf{K}_{\text{ext},12} & \mathbf{K}_{\text{ext},13} \\ \mathbf{0}_{3\times3} & \mathbf{K}_{\text{ext},22} & \mathbf{K}_{\text{ext},23} \\ \mathbf{0}_{1\times3} & \mathbf{K}_{\text{ext},32} & 0 \end{bmatrix}$$

with

$$\mathbf{K}_{\text{ext},12} = -\frac{1}{\|\mathbf{r}'\|^2}\hat{\bar{\mathbf{n}}}\cdot\hat{\mathbf{r}}', \quad \mathbf{K}_{\text{ext},13} = \frac{1}{\|\mathbf{r}'\|}\mathbf{r}'\times\bar{\mathbf{n}}$$

$$\mathbf{K}_{\text{ext},23} = -\frac{1}{\|\mathbf{r}'\|^3}\mathbf{r}'\times(\mathbf{r}'\times\bar{\mathbf{m}})$$

$$\mathbf{K}_{\text{ext},22} = \frac{1}{\|\mathbf{r}'\|^4}\hat{\mathbf{r}}'\cdot\hat{\bar{\mathbf{m}}}\cdot\hat{\mathbf{r}}' + \frac{1}{\|\mathbf{r}'\|^2}\hat{\bar{\mathbf{m}}} - \frac{2}{\|\mathbf{r}'\|^4}(\bar{\mathbf{m}}\times\mathbf{r}')\otimes\mathbf{r}'$$

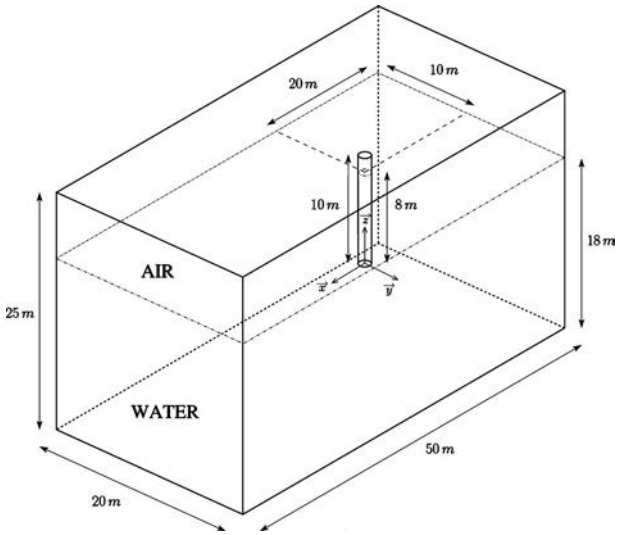

Fig. 12 Deformable cable partly in water

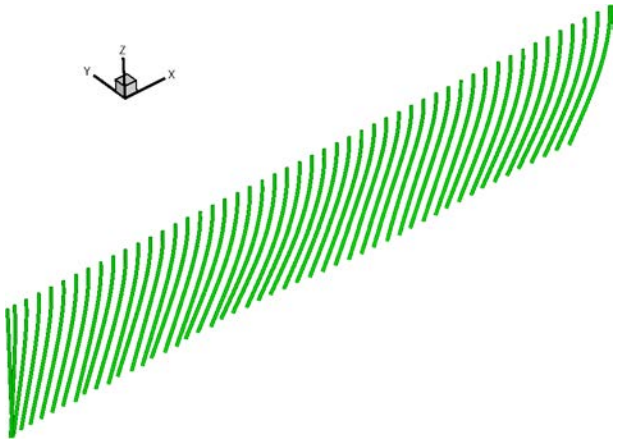

Fig. 14 Towed cable into a multifluid domain (snapshots every 0.5 s)

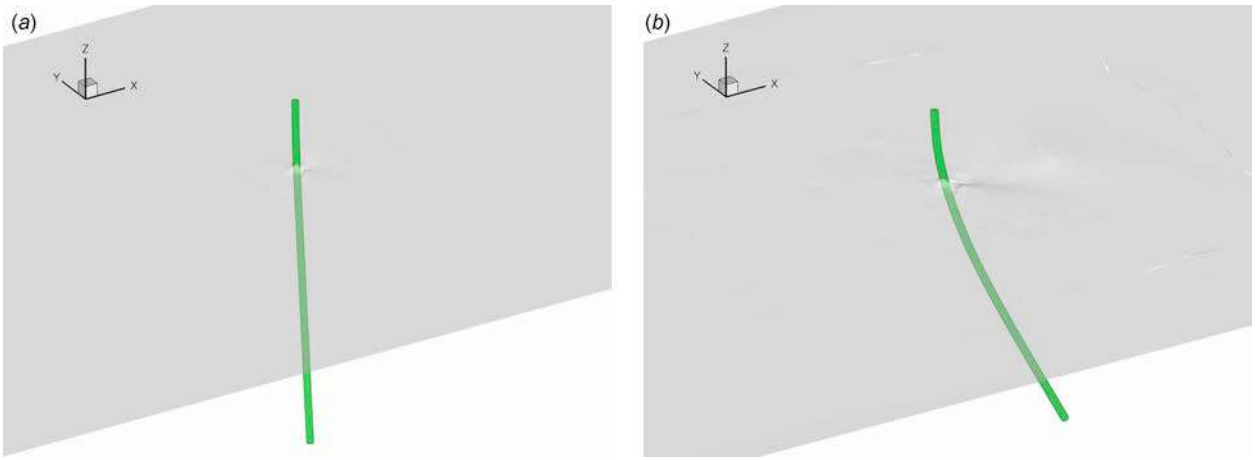

Fig. 13 Cable with inflow piercing the free surface: (*a*) initial configuration and (*b*) deformed cable at t=15 s

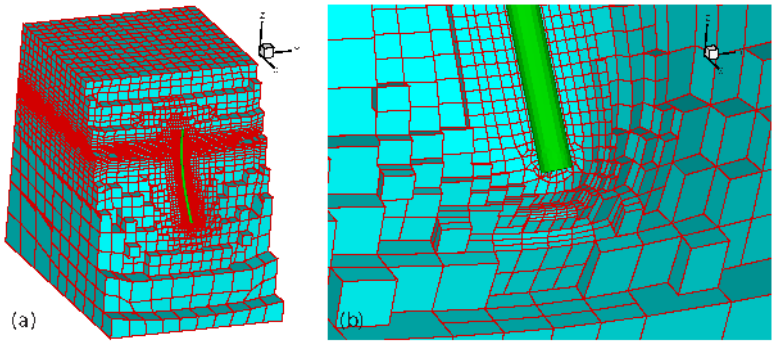

Fig. 15 Deformed mesh at t=15 s: (*a*) global view and (*b*) zoom at the free cable extremity

$$\mathbf{K}_{\text{ext},32} = -\frac{1}{\|\mathbf{r}'\|^3}\mathbf{r}'^T \cdot \hat{\bar{\mathbf{m}}} \cdot \hat{\mathbf{r}}' + \frac{1}{\|\mathbf{r}'\|}\bar{\mathbf{m}}^T - \frac{1}{\|\mathbf{r}'\|^3}(\mathbf{r}' \cdot \bar{\mathbf{m}}) \cdot \mathbf{r}'^T$$

Tangent stiffness of generalized constraint forces

$$\mathbf{K}_c = \left.\frac{d}{d\epsilon}\right|_{\epsilon=0} \mathbf{f}_{c,\epsilon} = \begin{bmatrix} \mathbf{0}_{3\times3} & \mathbf{0}_{3\times3} & \mathbf{0}_{3\times1} \\ \mathbf{0}_{3\times3} & (\lambda_\vartheta + p(\vartheta - \vartheta_d(t,X)))\boldsymbol{\pi}_n(X) & \mathbf{0}_{3\times1} \\ \mathbf{0}_{1\times3} & \mathbf{0}_{1\times3} & 0 \end{bmatrix}$$

where we introduce the differential of $\mathbf{u}_n$

$$\boldsymbol{\pi}_n(X) = \left(\mathbf{u}_n \otimes \left(-\frac{\mathbf{r}'}{\|\mathbf{r}'\|^2} - \frac{1}{(\|\mathbf{r}_n'\|\|\mathbf{r}'\| + \mathbf{r}_n' \cdot \mathbf{r}')} \left(\|\mathbf{r}_n'\| \frac{\mathbf{r}'}{\|\mathbf{r}'\|} + \mathbf{r}_n' \right) \right) + \frac{1}{\|\mathbf{r}'\|(\|\mathbf{r}_n'\|\|\mathbf{r}'\| + \mathbf{r}_n' \cdot \mathbf{r}')} \hat{\mathbf{r}}_n' \right)$$

References

[1] Cosserat, E., and Cosserat, F., 1909, Théorie des corps déformables, Hermann.

[2] Timoshenko, S. P., 1921, "LXVI. On the Correction for Shear of the Differential Equation for Transverse Vibrations of Prismatic Bars," Philosophical Magazine Series 6, **41**, pp. 744–746.

[3] Reissner, E., 1973, "On a One-Dimensional Large Displacement Finite-Strain Theory," Stud. Appl. Math., **52**, pp. 87–95.

[4] Simo, J. C., 1985, "A Finite Strain Beam Formulation. The Three-Dimensional Dynamic Problem. Part I: Formulation and Optimal Parametrization," Comput. Methods Appl. Mech. Eng., **49**, pp. 55–70.

[5] Simo, J. C., and Vu-Quoc, L., 1986, "A Three-Dimensional Finite-Strain Rod Model. Part II: Computational Aspects," Comput. Methods Appl. Mech. Eng., **58**, pp. 79–116.

[6] Simo, J. C., and Vu-Quoc, L., 1988, "On the Dynamics in Space of Rods Undergoing Large Motions—A Geometrically Exact Approach," Comput. Methods Appl. Mech. Eng., **66**, pp. 125–161.

[7] Cardona, A., and Gérardin, M., 1988, "A Beam Finite Element Non-Linear Theory With Finite Rotations," Int. J. Numer. Methods Eng., **26**, pp. 2403–2438.

[8] Cardona, A., Gérardin, M., and Doan, D. B., 1991, "Rigid and Flexible Joint Modelling in Multibody Dynamics Using Finite Element," Comput. Methods Appl. Mech. Eng., **89**, pp. 395–418.

[9] Ibrahimbegovic, A., Frey, F., and Kozar, I., 1995, "Computational Aspects of Vector-Like Parametrization of Three-Dimensional Finite Rotations," Int. J. Numer. Methods Eng., **38**, pp. 3653–3673.

[10] Ibrahimbegovic, A., 1997, "On the Choice of Finite Rotation Parameters," Comput. Methods Appl. Mech. Eng., **149**, pp. 49–71.

[11] Ibrahimbegovic, A., and Al Mikdad, M., 1999, "Finite Rotations in Dynamics of Beams and Implicit Time-Stepping Schemes," Int. J. Numer. Methods Eng., **41**, pp. 781–814.

[12] Ibrahimbegovic, A., and Mamouri, S., 2000, "On Rigid Components and Joint Constraints in Nonlinear Dynamics of Flexible Multibody Systems Employing 3D Geometrically Exact Beam Model," Comput. Methods Appl. Mech. Eng., **188**, pp. 805–831.

[13] Chrisfield, M. A., and Jelenic, G., 1999, "Objectivity of Strain Measures in the Geometrically Exact Three-Dimensional Beam Theory and Its Finite-Element Implementation," Proc. R. Soc. London, Ser. A, **455**, pp. 1125–1147.

[14] Kapania, R. K., and Li, J., 2003, "On a Geometrically Exact Curved/Twisted Beam Theory Under Rigid Cross-Section Assumption," Comput. Mech., **30**, pp. 428–443.

[15] Zupan, D., and Saje, M., 2003, "Finite-Element Formulation of Geometrically Exact Three-Dimensional Theories Based on Interpolation of Strain Measures," Comput. Methods Appl. Mech. Eng., **192**, pp. 5209–5248.

[16] Simo, J. C., Fox, D. D., and Rifai, M. S., 1990, "On a Stress Resultant Geometrically Exact Shell Model. Part III: Computational Aspects of the Non Linear Theory," Comput. Methods Appl. Mech. Eng., **79**, pp. 21–70.

[17] Love, A. E. H., 1944, *A Treatise on the Mathematical Theory of Elasticity*, 4th ed., Dover, New York.

[18] Burgess, J. J., 1993, "Bending Stiffness in a Simulation of Undersea Cable Deployment," Int. J. Offshore Polar Eng., **3**, pp. 197–204.

[19] Triantafyllou, M. S., and Howell, C. T., 1994, "Dynamics Response of Cables Under Negative Tension: An Ill-Posed Problem," J. Sound Vib., **173**(4), pp. 433–447.

[20] Sun, Y., and Leonard, J. W., 1998, "Dynamics of Ocean Cables With Local Low-Tension Regions," IEEE J. Ocean. Eng., **25**(6), pp. 443–463.

[21] Tjavaras, A. A., Zhu, Q., Liu, Y., Triantafyllou, M. S., and Yue, D. K. P., 1998, "The Mechanics of Highly-Extensible Cables," J. Sound Vib., **213**(4), pp. 709–737.

[22] Wang, P., Fung, R., and Lee, M., 1998, "Finite Element Analysis of a Three-Dimensional Underwater Cable With Time-Dependent Length," J. Sound Vib., **209**(2), pp. 223–249.

[23] Boyer, F., and Primault, D., 2004, "Finite Element of Slender Beams in Finite Transformations: A Geometrically Exact Approach," Int. J. Numer. Methods Eng., **59**, pp. 669–702.

[24] Meirovich, L., 1967, *Analytical Methods in Vibrations*, Macmillan, New York.

[25] Antman, S., 1972, *The Theory of Rods*, Springer, Berlin.

[26] Naghdi, P. M., 1980, "Finite Deformation of Elastic Rods and Shells," Proceedings of the IUTAM, Symposium on Finite Elasticity.

[27] Gamkrelidze, R. V., 1991, *Encyclopaedia of Mathematical Sciences, Vol. 28, Geometry I*, Springer-Verlag, Berlin.

[28] Simo, J. C., and Fox, D. D., 1989, "On a Stress Resultant Geometrically Exact Shell Model. Part I: Formulation and Optimal Parametrization," Comput. Methods Appl. Mech. Eng., **72**, pp. 267–304.

[29] Ibrahimbegovic, A., Brank, B., and Courtois, P., 2001, "Stress Resultant Geometrically Exact Form of Classical Shell Model and Vector Like Parametrization of Constrained Finite Rotations," Int. J. Numer. Methods Eng., **52**, pp. 1235–1252.

[30] Malvern, L. E., 1969, *Introduction to the Mechanics of a Continuous Medium*, Prentice-Hall, Englewood Cliffs, NJ.

[31] Gérardin, M., and Rixen, D., 1997, *Mechanical Vibrations: Theory and Application to Structural Dynamics*, Wiley, New York.

[32] Simo, J. C., and Wong, K. K., 1991, "Unconditionally Stable Algorithms for Rigid Body Dynamics That Exactly Preserve Energy and Momentum," Int. J. Numer. Methods Eng., **31**, pp. 19–52.

[33] Marsden, J. E., and Hughes, T. J. R., 1994, *Mathematical Foundations of Elasticity*, Dover, New York.

[34] Hilbert, H. M., Hughes, T. J. R., and Taylor, R. L., 1977, "Improved Numerical Dissipation for Time Integration Algorithms in Structural Dynamics," Earthquake Eng. Struct. Dyn., **5**, pp. 283–292.

[35] Wood, W. L., Bossak, M., and Zienkiewics, O. C., 1980, "An Alpha Modification of Newmark's Method," Int. J. Numer. Methods Eng., **15**, pp. 1562–1566.

[36] Chung, J., and Hulbert, G. M., 1993, "A Time Integration Algorithm for Structural Dynamics With Improved Numerical Dissipation: The Generalized-α Method," ASME J. Appl. Mech., **60**, pp. 371–375.

[37] Murray, R. M., Li, Z., and Sastry, S. S., 1994, *A Mathematical Introduction to Robotic Manipulation*, CRC, USA.

[38] Wall, W. A., and Ramm, E., 1998, "Fluid-Structure Interaction Based Upon a Stabilized (ALE) Finite Element Method," IV World Congress on Computational Mechanics, S. R. Idelsohn, E. Onate, and E. N. Dvorkin, eds.

[39] Huebner, B., Walhorn, E., and Dinkier, D., 2004, "A Monolithic Approach to Fluid-Structure Interaction Using Space-Time Finite Element," Comput. Methods Appl. Mech. Eng., **193**, pp. 2087–2104.

[40] De Nayer, G., 2008, "Interaction Fluide-Structure pour les corps élancés," Ph.D. thesis, Ecole Centrale Nantes, France. Available on-line: ftp://ftpa.ec-nantes.fr/user/ftp-emn/pub/Thesis/these_denayer.pdf

[41] de Boer, A., van Zuijlen, A. H., and Bijl, H., 2007, "Review of Coupling Methods for Non-Matching Meshes," Comput. Methods Appl. Mech. Eng., **196**, pp. 515–1525.

[42] Valdés Vázquez, J. G., 2007, "Nonlinear Analysis of Orthotropic Membrane and Shell Structures Including Fluid-Structure Interaction," Ph.D. thesis, Université polytechnique de Catalogne.

[43] Simo, J. C., Tarnow, N., and Wong, K. K., 1992, "Exact Energy-Momentum Conserving Algorithms and Symplectic Schemes for Nonlinear Dynamics," Comput. Methods Appl. Mech. Eng., **100**, pp. 63–116.

[44] Lewis, D., and Simo, J. C., 1994, "Conserving Algorithms for the Dynamics of Hamiltonian Systems on Lie Groups," J. Nonlinear Sci., **4**, pp. 253–299.

[45] Marsden, J. E., and West, M., 2011, "Discrete Mechanics and Variational Integrators," Acta Numerica, **10**, pp. 357–514.

[46] Leimkuhler, B., and Patrick, G. W., 1996, "A Symplectic Integrator for Riemannian Manifolds," J. Nonlinear Sci., **6**, pp. 367–384.